PURPOSE-LED PUBLISHING™

TOPICAL REVIEW • OPEN ACCESS

Quasi-bound states in the continuum for nonlinear applications in asymmetry metasurfaces

To cite this article: Wei Wu *et al* 2026 *J. Opt.* **28** 023001

View the article online for updates and enhancements.

You may also like

- Understanding and improving axial detection in optical tweezers based on the interference of forward- and backward-scattered light
Isaac Pérez Castillo, Simon Leturcq, Sylvain Domitin et al.
- Scattering in time-varying Drude–Lorentz models
Bryce Dixon, Calvin M Hooper, Ian R Hooper et al.
- Interaction mechanism between femtosecond laser and diamond
Jiecai Feng, Junzhe Wang, Cheng Li et al.

4-CHANNEL CONFIGURABLE OPEN RF ENGINE FOR QUANTUM EXPERIMENTS

LUGUS

Developed by Instrumentation Technologies

High bandwith arbitraty waveform generator (AWG)
Up to 1.25 GSPS

Open & programmable
Full access to FPGA implementation and firmware

Compatible with control frameworks
LabScript, ARTIQ, etc.

High power outputs
Up to 36 dBm

High-bandwidth feedback control
Open or closed-loop operation, Feedback bandwidth up to 125 MSPS

This content was downloaded from IP address 158.69.200.216 on 07/11/2026 at 05:25

IOP Publishing J. Opt. 28 (2026) 023001 https://doi.org/10.1088/2040-8986/ae4368

Journal of Optics

Check for updates

TOPICAL REVIEW

Quasi-bound states in the continuum for nonlinear applications in asymmetry metasurfaces

Wei Wu[1], **Zhuojun Liu**[2,*], **Guixin Qiu**[1], **Bo Chen**[1] and **Jin Liu**[1,2]

[1] State Key Laboratory of Optoelectronic Materials and Technologies, School of Physics, Sun Yat-sen University, Guangzhou 510275, People's Republic of China
[2] Quantum Science Center of Guangdong-Hong Kong-Macao Greater Bay Area, Shenzhen, People's Republic of China
[*] Author to whom any correspondence should be addressed.

E-mail: liuzhuojun@quantumsc.cn

OPEN ACCESS

RECEIVED
28 August 2025

REVISED
11 October 2025

ACCEPTED FOR PUBLICATION
9 February 2026

PUBLISHED
20 February 2026

Keywords: quasi-bound states in the continuum, asymmetry metasurfaces, nonlinear optics, high quality resonances

Original content from this work may be used under the terms of the Creative Commons Attribution 4.0 licence.

Any further distribution of this work must maintain attribution to the author(s) and the title of the work, journal citation and DOI.

Abstract

Asymmetry metasurfaces supporting quasi-bound states in the continuum (BIC) have recently emerged as a powerful platform for enhancing nonlinear optical processes by combining ultrahigh quality resonances with strong electromagnetic field confinement. Leveraging these unique properties, asymmetry metasurfaces have enabled significant advances in a broad range of nonlinear phenomena, including second- and third-harmonic generation, nonlinear chiral effects, high-harmonic generation, and spontaneous parametric down-conversion. Insights are also provided into several emerging research frontiers by asymmetry metasurfaces, such as adopting high-refractive-index materials, exploring novel quasi-BIC regulating mechanisms, and exploiting artificial intelligence–assisted inverse design for on-demand optimization. Looking ahead, broadband resonances control and novel material integration are anticipated to transform asymmetry metasurfaces into versatile, high-efficiency building blocks for compact and multifunctional nonlinear photonic devices.

1. Introduction

Nonlinear optical phenomena enable a broad range of applications, including telecommunications and all-optical data processing and storage [1, 2], spectroscopy [3, 4] and quantum information technologies [5, 6]. While these applications are promising, conventional nonlinear optical crystals typically exhibit intrinsically weak nonlinear responses, even under intense coherent excitation and with long interaction lengths [7]. This limitation has motivated extensive efforts to enhance nonlinear optical efficiency, particularly through nanophotonic platforms that offer stronger light–matter interactions and compact device footprint. For scalable integration, it is highly desirable for such devices to be compatible with standard complementary metal–oxide–semiconductor (CMOS) fabrication processes [7]. Metasurfaces have recently emerged as a promising class of planar nanophotonic platforms, enabling wavelength conversion and optical switching that can be employed in optical information processing for planar switching and routing elements [8, 9]. They overcome many limitations of conventional nonlinear materials by enabling subwavelength light manipulation and enhanced local electromagnetic fields.

Bound states in the continuums (BICs) have attracted particular attention due to their ability to greatly enhance light–matter interactions and thereby significantly boosting nonlinear optical responses in metasurfaces [10].The concept of BICs traces back to early studies by von Neumann and Wigner in 1929 [11], who theoretically predicted bound states with theoretically infinite lifetimes embedded within a continuum spectrum. Later developments in the 1960 s established BICs as a universal wave phenomenon arising from destructive interference between resonances, with experimental demonstrations achieved across various systems including electromagnetic, acoustic, and water waves [12–14]. In photonics, the theory of BICs was proposed in 2008 [15], and first experimentally realized in 2011 [16].

© 2026 The Author(s). Published by IOP Publishing Ltd

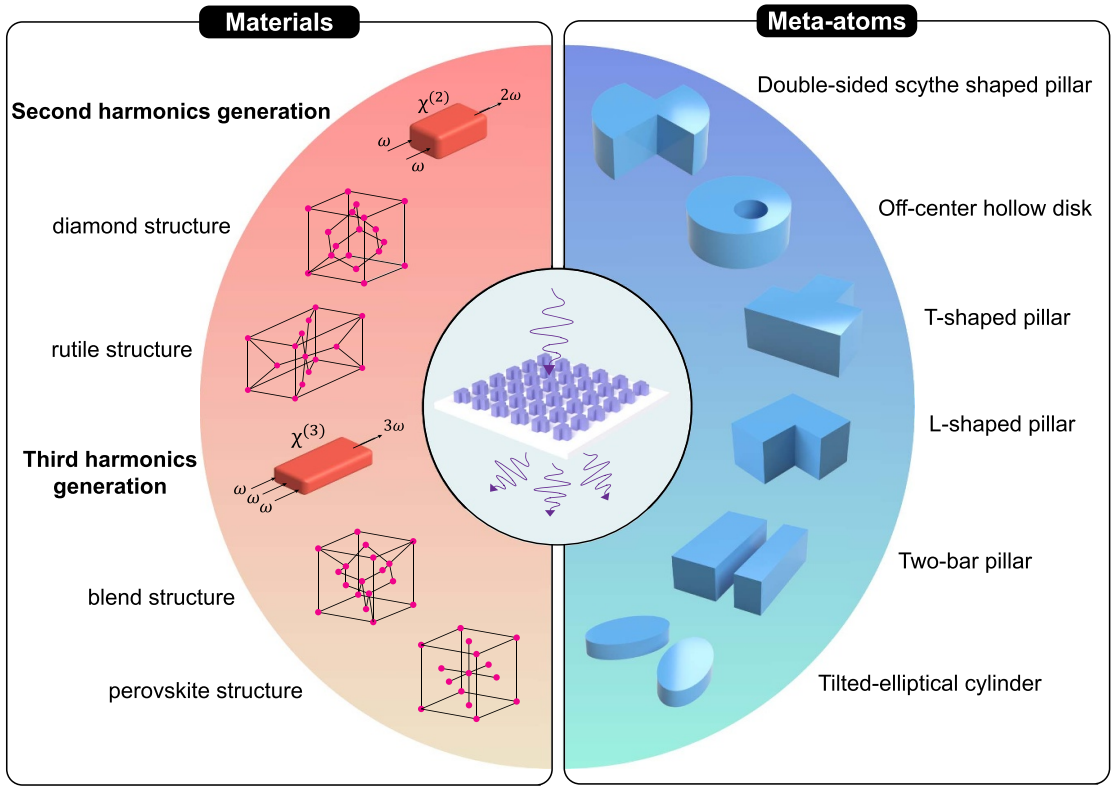


Figure 1. Synergistic strategy for constructing asymmetry metasurfaces: the left panel (material selection) illustrates representative materials applicable to second-harmonic generation (SHG) or third-harmonic generation (THG); the right panel (meta-atom design) presents representative asymmetric meta-atom designs.

While photonic structures such as waveguide arrays and metasurfaces have emerged as a reliable platform owing to the ability to tailor the materials and structures in recent years, they provide novel opportunities for realizing BICs in photonics, which is usually difficult in quantum system. Among these structures, asymmetry metasurfaces designed by introducing symmetry breaking can transform ideal BICs into quasi-BICs. These modified states retain ultrahigh quality factor (Q factor) characteristic while offering improved controllability. Importantly, quasi-BICs maintain accessibility to external excitation, thereby facilitating strong light-matter interactions that are particularly advantageous for nonlinear optical processes. Benefiting from their unique physical properties and compatibility with mature nanofabrication techniques, asymmetry metasurfaces have demonstrated their capability to mediate various nonlinear processes. Their tailored subwavelength architectures not only enhance fundamental nonlinear interactions but also allow advanced functionalities when incorporating anisotropic or chiral meta-atoms. These capabilities greatly expand the degrees of freedom for optical system design and offer new pathways towards compact, multifunctional photonic devices.

In this invited review, we systematically survey recent advances in asymmetry metasurface supporting quasi-BICs for enhanced nonlinear photonics, focusing on both material platforms and structural designs (see figure 1). The review is organized as follows: first, we introduce the theoretical basis of nonlinear optical processes and the analytical framework for BICs. Building upon these foundations, we then highlight the latest developments in asymmetry metasurfaces, with special emphasis on second-harmonic generation (SHG), third-harmonic generation (THG) nonlinear chiral effects, high-harmonic generation (HHG) and spontaneous parametric down-conversion (SPDC) for quantum applications. In each section, we compare the characteristics of different materials and discuss how asymmetry metasurface designs optimize nonlinear efficiency in their respective applications. Lastly, we propose three possible strategies that can help address the current limitations of Q factors and conclude with forward-looking perspectives in this field.

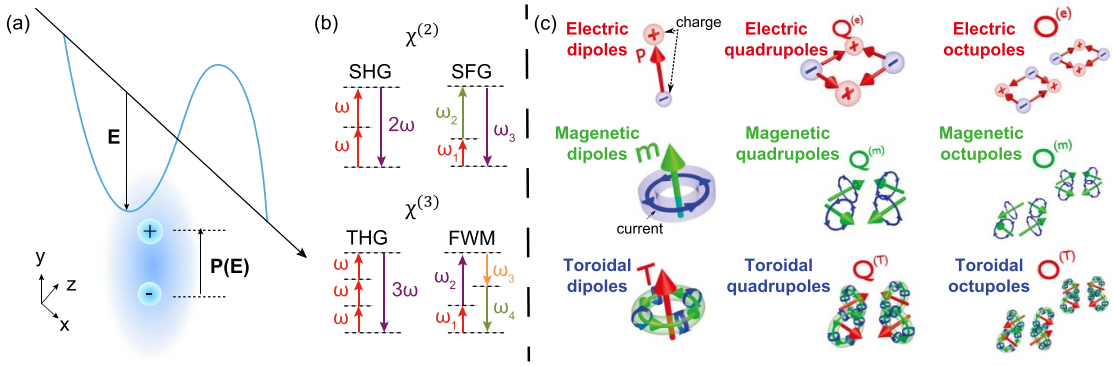


Figure 2. Illustration of theoretical basis: (a), (b) A dipole excitation and possible nonlinear process: (a) An electromagnetic wave with electric field E passing through an atom and thereby inducing a dipole oscillation P(E). (b) Second- and third-order nonlinear process drive by $\chi^{(2)}$ and $\chi^{(3)}$ respectively , showing SHG, SFG, THG, FWM (c)Three families of dynamic multipoles: the radiation field of meta-atoms can be decomposed into spherical harmonic vector components, with multipole expansion revealing the complete electromagnetic multipole construction and their far-field radiation patterns. Three rows show charge-current distributions that give rise to the electric dipoles (EDs), quadrupoles (EQs), octupoles (EOs); magnetic dipoles (MDs), quadrupoles (MQs), octupoles (MOs); and toroidal dipoles (TDs), quadrupoles (TQs), octupoles (TOs). (c) Reprinted figure with permission from [17], Copyright (2014) by the American Physical Society.

2. Theoretical background

2.1. Nonlinear principle

Nonlinear optical effects in metasurfaces arise from light-matter interactions, where the electric field of an optical signal couples with the outer-shell electrons of atoms, leading to a polarization response. As depicted in figure 2(a), a photon oscillating at frequency ω induces polarization by displacing an electron orbital with respect to the nucleus [18]. This polarization response can be characterized by the expansion of the non-linear susceptibility tensor [19]:

$$\mathbf{P} = \varepsilon_0 \left[\chi^{(1)}\mathbf{E} + \chi^{(2)} : \mathbf{EE} + \chi^{(3)} \vdots \mathbf{EEE} \right] \equiv \mathbf{P}^{(1)} + \mathbf{P}^{(2)} + \mathbf{P}^{(3)}. \quad (1)$$

Here, ϵ_0 is the vacuum permittivity, $\chi^{(1)}$ is the linear electric susceptibilities, $\chi^{(2)}$ and $\chi^{(3)}$ represent the second- and third-order nonlinear susceptibilities, respectively, and $\mathbf{E}$ is the local electric field. Typically, $\chi^{(n)}$ is a (n+1)-rank tensor, which depends on the crystal structure of a material. The first term $\mathbf{P}^{(1)}$ represents the linear polarization response while the remainders are the nonlinear components. The second term $\mathbf{P}^{(2)}$ represents second-order nonlinear processes including SHG and sum frequency generation (SFG), while the third term $\mathbf{P}^{(3)}$ governs third-order nonlinear processes including THG and four-wave mixing (FWM), as illustrated in figure 2(b). In conventional bulk nonlinear optical materials, these effects are intrinsically weak and require strict phase-matching conditions to accumulate nonlinear interactions over extended propagation distances (typically millimeters to centimeters). Phase-matching is necessary to maintain constructive interference rather than destructive interference of the generated nonlinear signals during propagation. However, due to material dispersion effects, ideal phase-matching conditions can generally only be realized within narrow spectral windows. Moreover, the long interaction lengths in bulk crystals introduce transmission losses, further constrain overall efficiency. Together, these limitations significantly restrict the performance and flexibility of conventional bulk materials in nonlinear applications.

Metasurfaces have emerged as a powerful platform that fundamentally overcomes the limitations of conventional bulk nonlinear materials, as their subwavelength thickness inherently relaxes phase-matching conditions and minimizes transmission losses. Designing efficient nonlinear metasurfaces requires careful consideration of all terms in equation (1). For $\chi^{(n)}$, selecting materials with high nonlinear susceptibilities to fabricate metasurfaces is a direct approach to improving efficiency. For even-order harmonic generation such as SHG, non-centrosymmetric materials with strong $\chi^{(2)}$ are essential. Gallium arsenide (GaAs)[20–25] and aluminum GaAs (AlGaAs)[26–34] are commonly employed in SHG process due to their high $\chi^{(2)}$. However, their significant absorption in the visible spectrum limits SHG conversion efficiency. In contrast, gallium phosphide (GaP)[35, 36] has a wide bandgap that can avoid such absorption, as well as lithium niobate ($LiNbO_3$)[37–40] with bandgap of 3.88 eV. Beyond these conventional bulk nonlinear materials, two-dimensional (2D) materials have emerged as a promising alternative platform for nonlinear optics, such as 3R-molybdenum disulfide (3R-MoS_2)[41–45], 3R-tungsten

Table 1. SHG and THG processes in all-dielectric metasurfaces.

Nonlinear process	Materials	Bandgap (eV)	Nonlinear susceptibility
SHG	GaAs	1.42 [59, 60]	$\lvert\chi^{(2)}_{36}\rvert = 340\,\mathrm{pm\,V^{-1}}$ (106 nm)[60, 61]
	AlGaAs	1.72 [59, 62]	$\lvert\chi^{(2)}_{36}\rvert = 320\,\mathrm{pm\,V^{-1}}$ (1064 nm) [63]
	GaP	2.70 [60, 64]	$\lvert\chi^{(2)}_{36}\rvert = 318\,\mathrm{pm\,V^{-1}}$ (852 nm)[61]
	$BaTiO_3$ (barium titanate)	3.10 [65–67]	$\lvert\chi^{(2)}_{31}\rvert = 28\,\mathrm{pm\,V^{-1}}$ (1064 nm)[60, 68]
	ZnO (zinc oxide)	3.10 [60, 69]	$\lvert\chi^{(2)}_{33}\rvert = 14\,\mathrm{pm\,V^{-1}}$ (1064 nm)[70]
	$LiNbO_3$	3.88 [60, 71]	$\lvert\chi^{(2)}_{33}\rvert = 51\,\mathrm{pm\,V^{-1}}$ (852 nm)[60, 61]
	a-SiC[a]	4.00 [72]	$\lvert\chi^{(2)}_{33}\rvert = 24\,\mathrm{pm\,V^{-1}}$ (1064 nm)[73]
	3R-MoS_2	1.65 [74, 75]	$\lvert\chi^{(2)}_{22}\rvert = 780\,\mathrm{pm\,V^{-1}}$ (1350 nm)[76, 77]
	3R-WS_2	1.77 [74]	$\lvert\chi^{(2)}_{22}\rvert = 500\,\mathrm{pm\,V^{-1}}$ (1058 nm)[78]
	ϵ-GaSe	2.30 [79]	$\lvert\chi^{(2)}_{33}\rvert = 2400\,\mathrm{pm\,V^{-1}}$ (1210 nm)[79]
THG	a-Si[a]	1.70 [80, 81]	$\chi^{(3)}_{1111} = 0.60\,\mathrm{nm^2\,V^{-2}}$ (1550 nm)[82, 83]
	c-Si[b]	1.12 [60, 80]	$\chi^{(3)}_{1111} = 0.25\,\mathrm{nm^2\,V^{-2}}$ (1550 nm)[84, 85]
	a-Ge	0.70 [86, 87]	$\chi^{(3)}_{1111} = 0.57\,\mathrm{nm^2\,V^{-2}}$ (1650 nm)[88, 89]
	As_2S_3	2.22 [60, 90, 91]	$\lvert\chi^{(3)}_{eff}\rvert = 0.44\,\mathrm{nm^2\,V^{-2}}$ (1550 nm)[90, 91]
	TiO_2	3.35 [60, 92]	$\chi^{(3)}_{1111} = 0.02\,\mathrm{nm^2\,V^{-2}}$ (1550 nm)[60, 93, 94]
	BP	1.60 [95]	$\lvert\chi^{(3)}_{eff}\rvert = 0.16\,\mathrm{nm^2\,V^{-2}}$ (1560 nm)[96]
	Graphene	0 [97]	$\lvert\chi^{(3)}_{eff}\rvert = 0.10\,\mathrm{nm^2\,V^{-2}}$ (1560 nm)[96]

[a] a represents amorphous.
[b] c represents crystalline.

disulfide (3R-WS_2)[46–48], ϵ-gallium selenide (ϵ-GaSe)[49–51]. They exhibit strong $\chi^{(2)}$ for SHG, and their atomic-scale thickness necessitates integration with resonant nanostructures to provide sufficient nonlinear interaction length. For odd-order harmonic generation such as THG, this process is not constrained by crystal symmetry, enabling the use of centrosymmetric semiconductors. Silicon (Si)[52–56] and germanium (Ge)[57] are particularly suitable due to their substantial third-order nonlinear susceptibility ($\chi^{(3)}$) in near-infrared (IR) wavelengths. Titanium dioxide (TiO_2)[58] is effective for THG in the visible and ultraviolet ranges, while arsenic sulfide (As_2S_3)[46] offers advantages in the mid-IR due to its strong nonlinearity and broad transparency window. Like in the SHG process, 2D materials such as black phosphorus (BP) and graphene also exhibit large $\chi^{(3)}$ for THG. Apart from materials discussed above, other commonly used materials and more detailed parameters are listed in table 1. Beyond material selection, metasurface designs must also account for the orientation of principal crystalline axes, as their alignment with the local electric field E will influence the polarization intensity P.

2.2. Enhancement mechanism

Among all parameters in equation (1), the electric field **E** plays a dominant role in enhancing nonlinear optical processes. This dependence becomes even more critical for high-order processes, as the nonlinear polarization scales with the nth power of **E**. Therefore, enhancing the local electric field within metasurfaces is a primary strategy for boosting nonlinear interactions. To achieve this enhancement, metasurfaces are often designed with subwavelength nanostructures that support resonant electromagnetic modes, facilitating strong field confinement. The electromagnetic multipole expansion provides a systematic framework for analyzing such resonances. According to multipolar expansion theory, the electromagnetic field of a resonance can be decomposed into contributions from electric modes, magnetic modes, and toroidal modes as visualized in figure 2(c), and each mode includes infinite orders, while the contribution of high-order modes is usually small enough to be ignored [17, 98, 99]. In Cartesian coordinates, the multipole response can be described by equations (2)–(7) [100, 101]:

$$\boldsymbol{P} = -\frac{1}{\mathrm{i}\omega}\int \boldsymbol{j}\,\mathrm{d}^3\boldsymbol{r} \tag{2}$$

$$\boldsymbol{M} = \frac{1}{2c}\int (\boldsymbol{r}\times\boldsymbol{j})\,\mathrm{d}^3\boldsymbol{r} \tag{3}$$

$$\boldsymbol{T} = \frac{1}{10c}\int \left[(\boldsymbol{r}\cdot\boldsymbol{j})\,\boldsymbol{r} - 2\boldsymbol{r}^2\boldsymbol{j}\right]\mathrm{d}^3 r \tag{4}$$

$$Q_{\alpha,\beta}^{(E)} = \frac{1}{\mathrm{i}2\omega}\int\left[r_\alpha j_\beta + r_\alpha j_\beta - \frac{2}{3}(\boldsymbol{r}\cdot\boldsymbol{j})\,\delta_{\alpha,\beta}\right]\mathrm{d}^3\boldsymbol{r} \tag{5}$$

$$Q_{\alpha,\beta}^{(M)} = \frac{1}{3c}\int\left[(\boldsymbol{r}\times\boldsymbol{j})_\alpha \boldsymbol{r}_\beta + (\boldsymbol{r}\times\boldsymbol{j})_\beta \boldsymbol{r}_\alpha\right]\mathrm{d}^3\boldsymbol{r} \tag{6}$$

$$Q_{\alpha,\beta}^{(T)} = \frac{1}{28c}\int\left[4r_\alpha r_\beta(\boldsymbol{r}\cdot\boldsymbol{j}) - 5r^2(r_\alpha j_\beta + r_\beta j_\alpha) + 2r^2(\boldsymbol{r}\cdot\boldsymbol{j})\,\delta_{\alpha,\beta}\right]\mathrm{d}^3\boldsymbol{r} \tag{7}$$

where $\boldsymbol{P}$ represents the electric dipoles (ED) moment, $\boldsymbol{M}$ represents the magnetic dipole (MD) moment, T represents the toroidal dipole (TD) moment, $Q_{\alpha,\beta}^{(E)}$ represents the electric quadrupole (EQ) moment, $Q_{\alpha,\beta}^{(M)}$ represents the magnetic quadrupole (MQ) moment, $Q_{\alpha,\beta}^{(T)}$ represents the TQ moment, c is the speed of light in vacuum, ω is the angular frequency, and $\boldsymbol{r}$ is the displacement vector from the origin to any point in space. $\alpha, \beta = x,y,z$ is the coordinate components. Therefore, the far field can be expressed as [100]:

$$\begin{aligned} I = {} & \frac{2\omega^4}{3c^3}|\boldsymbol{P}|^2 + \frac{2\omega^4}{3c^3}|\boldsymbol{M}|^2 + \frac{4\omega^5}{3c^4}\mathrm{Im}(\boldsymbol{P}\cdot\boldsymbol{T}) + \frac{2\omega^6}{3c^5}|\boldsymbol{T}|^2 \\ & + \frac{\omega^6}{c^5}\sum|Q_{\alpha,\beta}^{(E)}|^2 + \frac{\omega^6}{20c^5}\sum|Q_{\alpha,\beta}^{(M)}|^2 + o\left(\frac{1}{c^5}\right). \end{aligned} \tag{8}$$

Here, the first term means the far-field scattering energy of ED in the far field, the second term is the scattering energy of MD, the third term signifies the interference between ED and MD, the fourth term means the scattering energy of TD, and the fifth and sixth terms are the scattering energies of the EQ and the MQ, respectively. $o\left(\frac{1}{c^5}\right)$ represents the contribution of higher-order modes that are usually very small. The multipolar expansion theory thus provides an efficient approach for analyzing the scattering energies of the far field. Notably, in many cases these resonant modes will interact with each other to form a field enhancement mode. For example, when ED and TD satisfy a specific destructive interference condition($\boldsymbol{P} = -\mathrm{i}k\boldsymbol{T}$), their far-field radiation cancels out completely, forming a non-radiating anapole mode [102–104]. This results in significant suppression of far-field scattering while simultaneously enhancing near-field localization, effectively confining electromagnetic energy within the nanostructure. Another example arises when the ED spectrally overlaps with MD or TD, such interaction between bright and dark modes gives rise to Fano resonances characterized by sharp, asymmetric line shapes in the scattering spectrum [105–108]. These Fano resonances enable the formation of high-Q modes thus significantly enhance near-field localization.

Among all these Mie-type resonances, BICs stand out as the most intriguing one due to their unique physical characteristics (figure 3). BICs are non-radiative eigenmodes that exist within the radiation continuum but remain completely decoupled from it, thereby suppressing radiative losses and achieving theoretically infinite Q factors. Thus, they are ideal candidates for enhancing nonlinear optical processes [16, 111–113]. Furthermore, BICs are also topologically protected states that manifest as vortex singularities in momentum space (k-space)[114]. These singularities, known as V-points, are associated with far-field polarization vortices and characterized by a topological charge q, which describes the winding behavior of the polarization vector. The topological charge can be calculated as [115]:

$$q = \frac{1}{2\pi}\oint_C \mathrm{d}\mathbf{k}\cdot\nabla_{\mathbf{k}}\phi(\mathbf{k}), \qquad q\in\mathbb{Z} \tag{9}$$

where C is a closed loop in k-space that encircles the BIC in a counterclockwise direction, and $\phi(\mathbf{k}) = \arg\left[E_x(\mathbf{k}) + \mathrm{i}E_y(\mathbf{k})\right]$ is the polarization angle, with E_x and E_y are the complex amplitudes of the radiated plane waves. The value of q corresponds to the number of times the polarization vector rotates by 2π along the loop C (see in figure 3(e)).

From a theoretical standpoint, the analysis of BICs requires specialized analytical approaches. Time-domain coupled-mode theory describes a BIC as a non-radiative resonant state completely decoupled from radiation channels, exhibiting perfect energy confinement. From the perspective of symmetry theory, BICs occur when the modal symmetry of the resonant state is incompatible with that of the radiation continuum, thus preventing coupling. Alternatively, coupled-wave theory explains BICs as arising

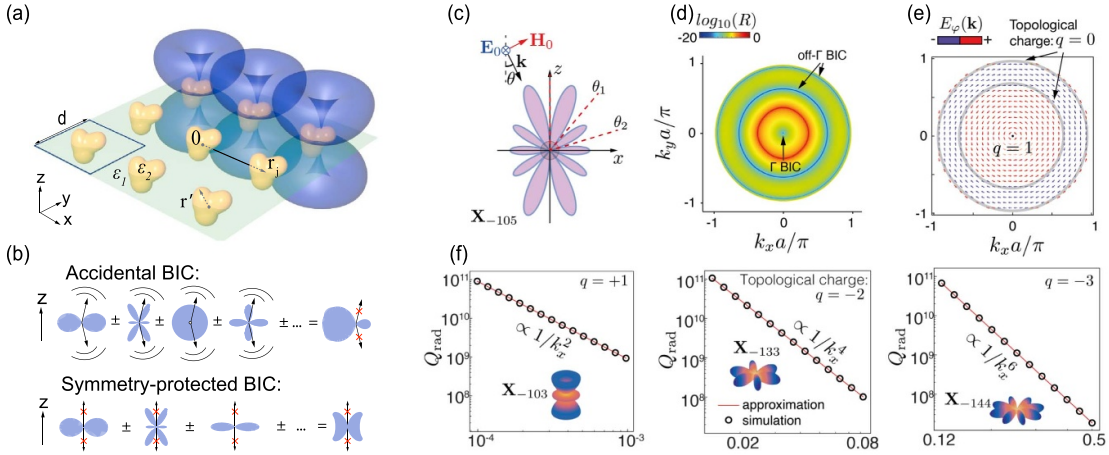


Figure 3. Diagram of BIC Mechanism. (a) Subsection of the metasurface with dielectric meta-atoms, used to illustrate multipolar characterization. (b) Schematic diagram of the formation of two types of BICs. (c) Far-field radiation pattern of the multipolar lattice ($l = 5, m = 0$) with inset showing the polarization of the incident wave. (d) Reflection map for the multipolar X_{-105} as a function of the in-plane wave vectors k_x and k_y. (e) Polarization map of the same lattice X_{-105} in the far field, revealing that BICs formatted with specific topological charge. (f) Numerical and analytical results for the asymptotic behavior of Q_{rad} near the Γ point with different topological charge, $q = +1, -2, -3$. (a), (b) Reprinted figure with permission from [109], Copyright (2019) by the American Physical Society. (c)–(f) Reprinted figure with permission from [110], Copyright (2022) by the American Physical Society.

from either vanishing modal coupling or destructive interference between resonant states. These theoretical frameworks, while offering valuable insights into BIC formation mechanisms from various perspectives, still remain limited in providing a more clear mathematical description. In contrast, the multipole expansion theory establishes a unified analytical framework that not only characterizes BIC phenomena but also maintains theoretical consistency with conventional Mie-type resonances. In this approach, the metasurface radiation field is expanded into a basis of vector spherical harmonics, as shown in figure 3(a), providing a rigorous theoretical framework that simultaneously accounts for both the periodic lattice arrangement and local resonator symmetries. Accordingly, the far-field radiation characteristics of a metasurface array can be formally expressed as [109]:

$$\mathbf{E}(\mathbf{r}) = E_0 \sum_{\mathbf{K},p_i,p_r,m,n} \widetilde{D}_{p_i,p_r,m,n} \frac{V_{\text{b}} \mathrm{i}^{-n}}{2\pi k_1} \int\int_{-\infty}^{\infty} \mathrm{d}k_{||} \delta\left(\mathbf{k}_b - \mathbf{k}_{||} - \mathbf{K}\right) \times \frac{\mathrm{e}^{\mathrm{i}\mathbf{k}\mathbf{r}}}{k_z} \left[\mathbf{Y}_{p_i,p_r,m,n}\left(\frac{\mathbf{k}}{|\mathbf{k}|}\right)\right]. \tag{10}$$

Here, $\mathbf{K}$ is the reciprocal lattice vector, $k_z = \pm\sqrt{k_1^2 - k_{||}^2}$, $|\mathbf{k}| = k_1 = \sqrt{\varepsilon_1}\frac{\omega}{c}$. And V_{b} is the volume of the first Brillouin zone. The spherical vector functions $\mathbf{Y}_{p_i,p_r,m,n}(\mathbf{n})$ depend on the spherical coordinates of a unity vector $\mathbf{n}$, where p_i, p_r, m, n are series of parameters used to present multipoles, and $\widetilde{D}_{p_i,p_r,m,n}$ is the amplitude corresponding to $\mathbf{Y}_{p_i,p_r,m,n}(\mathbf{n})$. Equation (10) rigorously correlates the multipolar radiation pattern of a single meta-atom with the collective far-field behavior of the metasurface. It offers powerful insight into the formation of BICs through multipolar coupling effects. This mechanism not only establishes fundamental criteria for the existence of bound states in photonic systems but also provides a novel paradigm for investigating BICs.

Clarifying the radiation images of different multipoles makes it easy to intuitively understand the formation of BICs. In subwavelength periodic arrays, the total radiation is a superposition of all multipolar contributions. Based on multipole expansion theory, BICs can arise under two distinct conditions (figure 3(b)):

(i) Accidental BICs: these arise when non-zero multipole components undergo complete destructive interference along the z-axis, effectively decoupling the system from free-space propagating light. These modes are referred to as 'accidental' because their positions in k-space occur at arbitrary positions, hence also known as off-Γ BICs. Especially, higher-order multipoles have a larger number of nodal lines that can form several off-Γ BICs, as illustrated in figure 3(c).
(ii) Symmetry-protected BICs: these arise when no multipolar component contributes to radiation along z-axis due to symmetry constraints. Specifically, as discussed in [109], multipole analysis reveals that in the sub-diffractive array, all modes lacking spherical harmonic with m $=$ 1 together form symmetry protected BICs. Especially, multipoles at the Γ point satisfy $m = 0$, where far-field radiation comprises multipoles without z-axis radiation components, hence also known as at-Γ BICs.

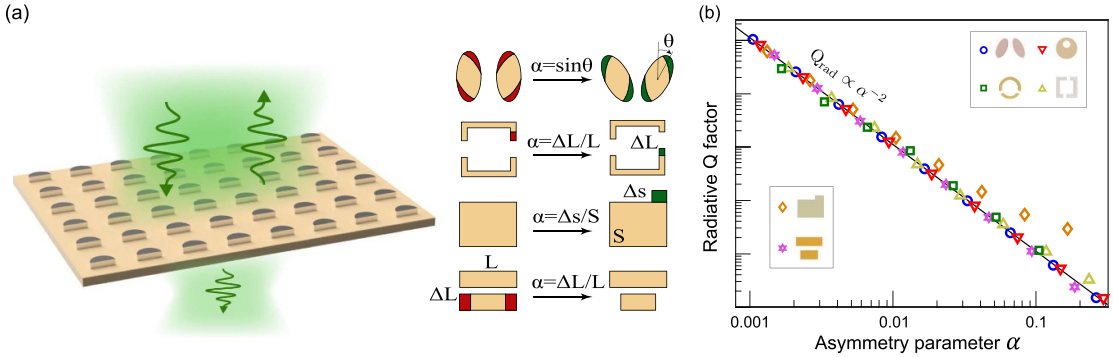


Figure 4. The symmetry breaking designs in metasurfaces and their effects on the Q_{rad}. (a) Concept schematic illustrating the normal incidence condition in asymmetry metasurfaces, and several usually applied asymmetric designs with their definitions of the asymmetry parameter α. (b) The effect of six types in-plane asymmetric designs on the Q_{rad}, showing that Q_{rad} depends on the asymmetry parameter α. Reprinted figure with permission from [120], Copyright (2018) by the American Physical Society.

The formation of both types of BICs in k-space is shown in figure 3(d). Notably, when considering the multipoles with rotational symmetry ($m = 0$), the accidental BICs (off-Γ BICs) constitute a closed continuous line in k-space, whereas symmetry-protected BICs (at-Γ BICs) emerges exclusively at the center as a singular point.

Symmetry-protected BICs formatted at the Γ point are particularly important in this review. In practical applications, their local Q factor scaling behavior near the Γ point is essential for assessing robustness to structural imperfections. Evaluating how rapidly the Q factor decreases away from the Γ point provides essential insight into the feasibility of high-Q mode engineering. A key step in this analysis is to establish a direct correlation between the topological charge q of the BIC and the local asymptotic scaling behavior of the Q. For multipolar lattices, the dependence of Q on the Bloch wave vector $k_b = (k_x, k_y, k_z)$ in the investigated system can be analytically determined through this defining expression: $Q = \omega W_{st}/P$, where W_{st} is the stored energy within a unit cell, P is the power radiated by the unit cell. It can be proved that, the asymptotic behavior of the Q factor near BICs is completely defined by the topological charge q of the BICs [110]:

$$Q \sim \frac{1}{|\mathbf{Y}_{p_i,p_r,m,n}(\mathbf{k}/|\mathbf{k}|)|^2} \sim \frac{1}{|\mathbf{k}_b|^{2|q|}} \tag{11}$$

Where $\mathbf{Y}_{p_i,p_r,m,n}(\mathbf{k}/|\mathbf{k}|)$ is the spherical vector functions mentioned in equation (10), and q is the topological charge defined in equation (9). This expression implies that the higher value of $|q|$, the slower the Q factor decreases with increasing distance from the Γ point in k-space. As illustrated in figure 3(f), when the topological charge takes values of $q = +1, -2, -3$, the system with larger topological charge shows a more gradual decrease of Q as further away from Γ point. This observed trend directly suggests that the magnitude of topological charge represents an indicator of structural robustness. This principle provides an important theoretical basis for a deeper understanding of the physical mechanism of BICs and the engineering design of high-Q modes on all dielectric metasurfaces.

The exceptional nonlinear enhancement of BICs-based metasurfaces originates from their high-Q resonance properties. BICs theoretically possess an unbounded Q factor, which stems from their perfect suppression of radiative losses in far field. However, such complete decoupling from far-field radiation makes BICs fundamentally inaccessible to external excitation. To overcome this limitation, it is necessary to introduce asymmetry into the system, thereby transforming an ideal BIC into a quasi-BIC. These quasi-BICs retain the essential features of high field confinement and enhanced light–matter interactions, while allowing finite but high Q factors. Recent studies have demonstrated that metasurfaces composed of arrays of symmetry-broken meta-atoms under normal incidence conditions can support quasi-BIC resonances with $Q = Q_{rad} + Q_{fab}$, where Q_{rad} is the radiative Q factor and Q_{fab} is the fabrication-induced Q factor. The maximal field enhancement is achieved for:

$$Q_{rad} = Q_{fab} \tag{12}$$

which is often termed as the critical coupling condition [116–119]. Through defining an asymmetry parameter α, work by Koshelev *et al* [120]. demonstrated a universal behavior for the Q_{rad} as a function

Table 2. Summary of the experimental Q factor of quasi-BICs in different nanostructures.

Methods	Structures	λ (nm)	Q
In-plane asymmetry perturbation	Si tilted-elliptical cylinders [131]	860	144
	Si metasurface with hybridization of two lattices [128]	1540	700
	GaAs L-shaped pillar [132]	1512	1000
	Si nanodisk dimer [133]	1480	3142
	Si U-shaped pillar [134]	1548	3534
	Si metasurface with hybridization of two lattices [129]	1513	4130
	Si off-center hollow square [135]	1500	4990
	Si T-shaped pillar [136]	1588	18 511
	Si double-holes [137]	1553	36 964
	Shallow Si pair-rod [138]	1560	101 486
	Si composite slites [139]	1503	110 510
Out-of-plane asymmetry perturbation	TiO_2 slant bar [140]	613	1250
	TiO_2 slant square nanohole [141]	618	2663
Permittivity perturbation	Si/TiO_2 hybridized metasurface [130]	1485	40

of α for all studied asymmetry metasurfaces (figure 4). Figure 4(b) presents a direct comparison of the Q_{rad} as functions of the asymmetry parameter α in dielectric and plasmonic metasurfaces. Remarkably, despite their structural diversity, quasi-BICs systems exhibit a clear inverse quadratic scaling that is [116, 120]:

$$Q_{rad} = Q_0 \alpha^{-2}, \tag{13}$$

where Q_0 is a constant determined by the asymmetry metasurface design being independent of α. For larger α, Q_{rad} decreases faster because the deviation from the symmetric unit cell can not be considered as a weak pertubation. thereby validating the universality of this quasi-BIC model across different resonator configurations. Therefore, Q_{rad} can be tuned to match Q_{fab} which is determined by the manufacturing process and material properties to satisfy the critical coupling condition in equation (12).

Such relationship between Q factor and asymmetry offers a powerful and unified theoretical framework for designing high-Q resonant asymmetry metasurfaces via symmetry-breaking engineering. Among various symmetry-breaking strategies, the most widely adopted approach involves in-plane geometric perturbations to the meta-atom design. Typical types of meta-atoms (figure 4(a)) include asymmetric pairs of tilted elliptical cylinders [121, 122], square split-ring resonators [123, 124], L-shaped resonators [125, 126], two parallel nanobars with different lengths. In addition to in-plane symmetry breaking, another promising strategy involves out-of-plane symmetry breaking, which is realized by breaking the vertical symmetry. For instance, by varying the height of individual meta-atoms within the unit cell [127]. This approach allows for enhanced tunability without altering the lateral pattern layout, and is especially relevant in multilayered or 3D-integrated metasurfaces. Except for regulating geometric asymmetry, another method is to introduce hybridization of two lattices in the metasurface, which involves two different size of meta-atoms in each lattice [128] or two lattice hybridizated with different spacings [129]. More recently, alternative schemes have emerged that utilize permittivity perturbation wherein different materials are integrated in a unit cell [130]. This approach mitigates the fabrication challenges inherent to geometric asymmetry while preserving high-Q resonances. A representative summary of recent studies about breaking symmetry to form quasi-BICs are listed in table 2.

3. SHG

SHG is a second-order nonlinear optical process in which two photons at the fundamental frequency are coherently converted into a single photon at twice the frequency. This process requires a non-zero second-order nonlinear susceptibility $\chi^{(2)}$, which is intrinsically forbidden in centrosymmetric media under the electric-dipole approximation. As a result, efficient SHG occurs in materials with non-centrosymmetric crystal structures. Combining with asymmetry designs in metasurfaces can further enhance the SHG efficiency by supporting high-Q quasi-BICs. Absolute conversion efficiency of SHG is defined as the SHG power normalized to the average pump power at the fundamental frequency: $\eta_{SHG} = P_{2\omega}/P_{\omega}$.

GaAs and AlGaAs are particularly attractive for resonant SHG due to their high $\chi^{(2)}$ values and compatibility with nanofabrication. A representative work by Vabishchevich *et al* [126]. reports design

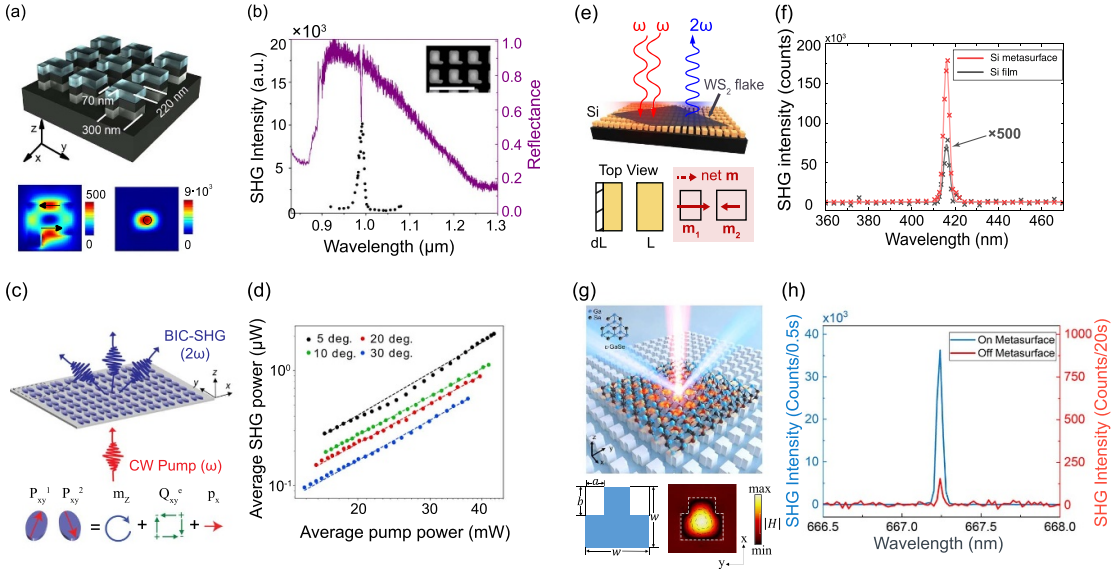


Figure 5. Nonlinear asymmetry metasurfaces for SHG. (a), (b) Vabishchevich's demonstration of enhanced SHG from a L-shaped GaAs metasurface: (a) GaAs asymmetry metasurface, based on a cube with a 300 nm side that has a notch cut form the corner, with the simulated electric (left) and magnetic (right) intensity profiles in the x–y horizontal plane shown below, and arrows indicate the directions of electromagnetic field vectors inside the nanoresonator. (b) Reflectivity spectrum of the L-shaped GaAs metasurface, indicating a high-Q resonance with a ∼2 nm spectral width, and the resonantly enhanced SHG at the Fano resonance wavelengths. (c), (d) Anthur's realization of highly efficient SHG from a tilted-elliptical cylinder Gap metasurface: (c) Conceptual illustration of SHG enhanced by quasi-BICs in a GaP asymmetry metasurface with Si substrate comprising a square lattice of dimers formed by two elliptical cylinders, with inset below showing the formation of the quasi-BICs. A single in-plane ED is induced in each particle in the dimer, containing x- and y-components $p^i_{x,y}$ (d) Experimentally measured power dependences of SHG from the tilted-elliptical cylinder metasurface. Experimental data is shown as dots and fits to the equation $P_{\mathrm{SHG}} = aP^b_{\mathrm{pump}}$ which is shown as dashed lines. (e), (f) Bernhardt's work to demonstrate enhanced SHG from a two-bar Si metasurface combined with a WS_2 monolayer: (e) Schematic of SHG from a WS_2 monolayer placed on top of the two-bar Si metasurface hosting BICs, with the unit cell asymmetry design shown below. The paired Si resonators in the cell exhibit MD moments $\boldsymbol{m_1}$ and $\boldsymbol{m_2}$, together generate a net MD moment m (f) Measured SH intensity from WS_2 monolayer on the two-bar Si metasurface (red) and on a reference bulk Si film (black, and magnified 500 times) (g), (h) Liu's demonstration of a giant SHG enhancement in a T-shaped Si metasurface coupled by GaSe flake: (g) Illustration of SHG from a GaSe flake laid on the surface of the T-shaped Si metasurface. Inset shows the lattice structure of ϵ-GaSe flake. Diagram below shows the T-shaped meta-atom with width w and asymmetry parameter a and b (left), and simulated magnetic field distribution (right) of the T-shaped Si metasurface. (h) Experimentally measured spectra of the SHG intensity from GaSe flake on and off the metasurface. (a), (b) Reprinted with permission from [126]. Copyright (2018) American Chemical Society. (c), (d) Reprinted with permission from [142]. Copyright (2020) American Chemical Society. (e, f) Reprinted with permission from [117]. Copyright (2020) American Chemical Society. (g), (h) Reprinted with permission from [143]. Copyright (2021) American Chemical Society.

of a GaAs metasurface composed of arrays of L-shaped nanoresonators with broken mirror symmetry to support high-Q Fano resonances, as shown in figure 5(a). The Fano resonance arises from the interference between a broad scattering continuum and a symmetry-protected dark mode BIC. Specifically, an out-of-plane MD becomes accessible by breaking the in-plane structural symmetry. This symmetry breaking enables coupling between the MD mode and free-space radiation, giving rise to a sharp spectral feature with a Q factor of approximately 500 and a linewidth of 2 nm near 0.98 μm. At the resonance wavelength, strong field localization occurs inside the GaAs nanoresonators, leading to a dramatic enhancement of the SHG. Experimentally, the SHG signal under resonant excitation is approximately 300 times stronger than that under off-resonant pumping. A SHG conversion efficiency of $\sim 6 \times 10^{-5}$ at pump intensity 3.1 GW cm^{-2} was achieved, as show in figure 5(b).

Despite these advantages, GaAs and AlGaAs suffer from strong absorption in the visible range of the spectrum that hinders the generated nonlinear frequencies. In contrast, GaP offers a wider bandgap and a broad transparency range from the visible to near-IR, making it more suitable for visible-wavelength SHG. Recent studies have explored GaP metasurfaces to exploit this advantage [144, 145]. Notably, Anthur *et al* [142]. demonstrated a GaP metasurface composed of a square array of nanodimers comprising two tilted elliptical cylinders to support high-Q quasi-BICs, as illustrated in figure 5(c). Figure 5(c) schematically depicts the unit cell of the tilted-elliptical cylinder metasurface and the relevant optical modes involved in the formation of the quasi-BIC. The unit cell consists of a pair of elliptical cylinders rotated by an angle θ relative to the vertical axis. When $\theta = 0°$, the structure exhibits a true BIC, resulting from the in-phase collective oscillation of an out-of-plane MD (m_z) and an in-plane electric quadrupole (Q^e_{xy}) . Breaking the symmetry ($\theta \neq 0°$) introduces a finite x-directed ED (p_x) , which mediates coupling between the localized state and the free-space continuum, thus forming

a quasi-BIC. Due to symmetry constraints, p_x is the only component that can couple to the incident x-polarized plane wave, enabling enabling external excitation of the high-Q resonance. And the metasurface was evaluated for SHG using both pulsed and continuous wave (CW) illumination. Remarkably, a record-high conversion efficiency of 2×10^{-7} was achieved under pump with intensities of $1\,\mathrm{kW\,cm^{-2}}$, see figure 5(d) for SHG power dependence curves at different θ, highlighting the resonant enhancement enabled by symmetry breaking. Another highly nonlinear material with relatively large bandgap is $LiNbO_3$, which enables SHG in the visible spectrum. A resonant nonlinear metasurface based on thin-film $LiNbO_3$ attained a high conversion efficiency of $\sim10^{-6}$ at $4.3\,\mathrm{GW\,cm^{-2}}$ average power, highlighting the potential of $LiNbO_3$ for integrated nonlinear optics [146]. Later work further reported an intriguing polarization behavior of the emitted SH [147], making z-cut $LiNbO_3$ metasurfaces promising tools for nonlinear holography with polarization encoding. Nevertheless, due to the inherent nanofabrication complexity of $LiNbO_3$, the realization of quasi-BIC resonances with high Q factors has not yet been fully achieved. Therefore, further advancements in $LiNbO_3$ nanofabrication techniques are crucial for unlocking the full potential of BIC-enhanced nonlinear metasurfaces based on $LiNbO_3$ platform.

While the discussed noncentrosymmetric materials exhibit strong intrinsic nonlinearities and have enabled efficient harmonic generation through resonant metasurfaces, their integration into practical photonic circuits remains limited. A major bottleneck lies in their incompatibility with CMOS fabrication processes. In contrast, centrosymmetric materials like Si are fully CMOS-compatible. However, the inversion symmetry of Si prohibits bulk second-order nonlinear responses under the electric-dipole approximation. A promising solution is to integrate 2D materials with Si asymmetry metasurfaces. These hybrid platforms leverage the strong $\chi^{(2)}$ nonlinearity of 2D materials and the field-enhancement capabilities of resonant Si metasurfaces, providing an elegant route to unlock SHG in centrosymmetric photonic systems.

Monolayer WS_2 is a favorable 2D material for SHG due to its strong nonlinear susceptibility, making it ideally suited for integration with nanophotonic platforms. A pioneering study by Bernhardt *et al* [117], marked a significant step forward by demonstrating the first hybrid metasurface that effective harnesses the nonlinear properties of a monolayer WS_2 through quasi-BIC engineering. Designed meta-atom comprises two parallel nanobars with a controlled width difference (dL), and the asymmetry parameter α is defined as the ratio of dL to the width of the larger nanobar (L) (figure 5(e)). With systematically varying dL, the researchers demonstrated precise control over α. As mentioned in equation (13), Q_{rad} directly depends on α. By fabricating a series of two-bar metasurfaces with varying α parameters, they achieved optimal SH intensity enhancement under critical coupling condition in equation (12). Experimental results reveal that the metasurface that features a 140 nm nanobar width ($\alpha = 0.22$) exhibits maximal enhancement, demonstrating a remarkable 1140-fold increase in SH generation from the coupled monolayer WS_2 relative to an unpatterned Si substrate as shown in figure 5(f). This work demonstrated the feasibility of integrating 2D materials with CMOS-compatible metasurfaces for efficient SHG. Building upon this foundational work, subsequent efforts have explored alternative 2D materials and symmetry-breaking strategies to further improve SHG performance on Si platforms. Liu *et al* [143]. introduced a more effective symmetry-breaking mechanism by designing T-shaped Si meta-atoms that support quasi-BIC resonances with higher Q factors. As illustrated in figure 5(g), the T-shaped metasurface incorporates a GaSe flake exhibiting strong nonlinear response. GaSe represents another promising type of 2D nonlinear materials. The second-order nonlinear response of GaSe increases with their thickness within one coherent length, and its $\chi^{(2)}$ can reach $\sim1000\,\mathrm{pm\,V^{-1}}$ [79]. The structural asymmetry, characterized by width w along with two asymmetry parameters (a and b), effectively breaks rotational symmetry, enabling quasi-BICs with Q factors exceeding 8900. These quasi-BIC modes exhibit MD characteristics with its dipole moment along the Z axis, which has been demonstrated to significantly enhance nonlinear light-matter interactions as shown in inset in figure 5(g). Under continuous-wave excitation resonant with the quasi-BIC mode, the system achieves a remarkable 9400-fold SHG enhancement compared to GaSe on unpatterned substrates (figure 5(h)). This approach not only surpasses earlier designs in terms of Q factor and field confinement, but also establishes a CMOS-compatible route for achieving efficient nonlinear light generation under low-power, continuous-wave operation.

This section presents a concise overview of SHG in asymmetry metasurfaces, with particular focus on diverse material platforms including GaAs, GaP, and 2D materials integrated with Si-based metasurfaces, such as monolayer WS_2 and GaSe flakes. Despite these advancements, the asymmetry metasurfaces for SHG applications continues to explore a wide range of promising material platforms, each offering unique advantages for optimizing nonlinear optical responses. As mentioned in table 1, traditional nonlinear oxides such as $BaTiO_3$, with their exceptional nonlinear coefficients ($|\chi^{(2)}_{31}| = 28\,\mathrm{pm\,V^{-1}}$), featuring both wide bandgap (3.1 eV) and intrinsic non-centrosymmetric perovskite structure, provide

robust foundations for combining with quasi-BIC field confinement effects. Similarly, ZnO features a wide bandgap (3.1 eV), high nonlinear susceptibility ($|\chi_{33}^{(2)}| = 14.4\,\mathrm{pm\,V^{-1}}$), and the unique ability to maintain substantial nonlinear responses in the vacuum ultraviolet (VUV) regime. Notably, Semmlinger *et al* [148]. have demonstrated a ZnO metasurface designed for nonlinear optical generation of VUV light, paving the way for compact and efficient VUV sources with potential applications in emerging technologies. Besides, chalcogenides are promising dielectric materials for nonlinear photonics due to their compositional tunability, the noncentrosymmetry of certain crystalline phases, and their suitability for nanostructuring in diverse architectures. As discussed by Das Gupta *et al* [149], they demonstrated a significant SHG within selenium (Se)-based metasurfaces, highlighting the potential of chalcogenides for engineering highly efficient and tailorable nonlinear optical devices.

Future research challenges remain in optimizing the interplay between material bandgaps and quasi-BIC resonances to simultaneously suppress absorption losses and maximize field enhancement. Another critical direction lies in the development of robust heterogeneous integration strategies that maintain both the high nonlinearity of the 2D material and the high Q factor of the asymmetry metasurfaces. Moreover, a deeper understanding of the ultrafast dynamics between the temporal confinement of quasi-BIC modes and the nonlinear response times of the constituent materials is essential for advancing device performance. Continued investigations along these lines are expected to yield new physical insights and drive further improvements in SHG efficiency and functionality.

4. THG

THG, a representative third-order nonlinear optical process, involves the frequency upconversion of incident photons to produce coherent radiation at exactly triple the fundamental frequency via $\chi^{(3)}$ nonlinear interactions. Unlike second-order effects, third-order nonlinearities are not forbidden in centrosymmetric media, allowing both crystalline and amorphous materials to be explored for THG applications. High-index and mid-index dielectric materials are already being explored for THG at subwavelength scale, including Si, Ge, AlGaAs. Among them, Si is still more applied in asymmetry metasurfaces for THG applications due to its compatibility with standard CMOS fabrication processes, lower manufacturing costs, and mature nanofabrication techniques that allow precise control of subwavelength features. Beyond material selection, careful structural optimization of asymmetry metasurfaces is equally critical for enhancing THG absolute conversion efficiency, that is defined as the radiated THG power normalized to the average pump power at the fundamental frequency: $\eta_{\mathrm{THG}} = P_{3\omega}/P_{\omega}$. This can be achieved by engineering the meta-atom geometry to control multipolar resonances, to suppress radiative losses and maximize Q factors through BICs. Si metasurfaces exploiting BICs have demonstrated THG efficiency improvements of several orders of magnitude compared to conventional nanostructures.

A landmark demonstration of THG enhancement in Si metasurfaces leveraging BIC physics was reported by Liu *et al* [136], marking the first realization of an ultrahigh-Q quasi-BIC resonance on Si metasurfaces. In this work, the authors designed a metasurface composed of T-shaped meta-atoms, formed by selectively removing identical volumes of material from each unit cell (figure 6(a)). Crucially, the structure preserves mirror symmetry with respect to the XZ plane, which suppresses radiative losses and enables the formation of a symmetry-protected quasi-BIC mode with a record-high Q factor of 18 511–the highest ever reported for a Si-based metasurface at the time. Furthermore, this mirror symmetry-preserving architecture enables significant nonlinear optical effects. The metasurface achieves a THG conversion efficiency of approximately 10^{-6} at $0.1\,\mathrm{GW\,cm^{-2}}$ pump intensity, representing an enhancement exceeding five orders of magnitude compared to a bare Si film of equivalent thickness, with a clear comparison shown in figure 6(b). Moreover, the device produces pronounced SHG, despite centrosymmetric structure of Si typically prohibiting second-order nonlinear effects. The THG and SHG are further verified by the power-dependent double logarithmic plots, with figure 6(c) clearly showing the expected cubic and quadratic scaling respectively.

While ultrahigh-Q resonances are critical for enhancing nonlinear processes, Q factor alone does not fully determine the efficiency of frequency conversion. Koshelev *et al* [116]. suggest and develop a novel concept that the interaction of Q_{rad} and Q_{fab} can regulate the THG intensity and optimal frequency conversion efficiency in asymmetry metasurfaces is attained when these two Q factors achieve balanced contributions through critical coupling conditions in equation (12). In this study, the authors designed meta-atoms consisting of asymmetric bar pairs with width variations δw (inset in figure 6(d)) and define an asymmetry parameter α as $\alpha = \delta\mathrm{w}/\mathrm{w}$, where w represents the width of the wider bar to experimentally validate this concept. To further study the matching mechanism between Q_{rad} and Q_{fab}, a series of six such two-bar Si matasurfaces with different α were fabricated, and they test out that Q_{rad} shows a direct dependence on α as mentioned in equation (13) (figure 6(e)). The experimental results,

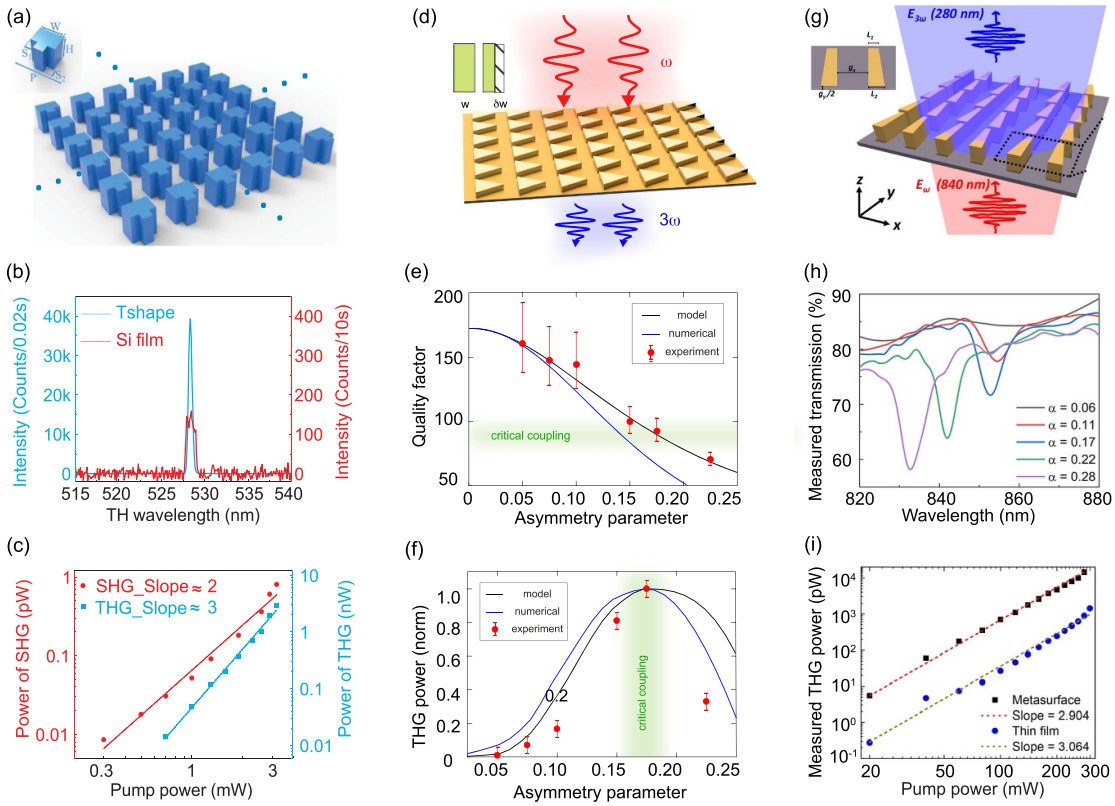


Figure 6. Nonlinear asymmetry metasurfaces for THG. (a)–(c) Liu's demonstration of SHG and THG from a T-shaped Si metasurface: (a) Schematic of the metasurface composed of Si cubes with asymmetric defects supporting quasi-BIC resonances. Inset: geometry of the T-shaped meta-atom. (b) Comparison of THG spectra between the T-shaped metasurface and a reference Si film of the same thickness. (c) Power dependence of SHG and THG signals, exhibiting quadratic and cubic scaling, respectively. (d)–(f) Koshelev's investigation of critical coupling–enhanced THG in a two-bar Si metasurface: (d) Conceptual illustration of THG enhancement in an asymmetric dielectric metasurface. Inset: unit cell design with definitions of the asymmetry parameter $\alpha = \delta w/w$. (e) Dependence of the Q on α, showing experimental results (red dots), numerical simulations (blue line), and analytical model predictions (black line). The shaded region marks the critical coupling regime. (f) THG power as a function of α, with maximum conversion efficiency achieved near $\alpha \approx 0.2$. (g)–(i) Abdelraouf's realization of (deep ultraviolet) DUV THG from a mirrored-trapezoidal c-Si metasurface: (g) Schematic of the c-Si metasurface on a sapphire substrate, pumped at 840 nm to generate transmitted THG at 280 nm. Inset: geometric parameters of the mirrored rignt-angle trapezoidal cell. (h) Measured transmission of the mirrored-trapezoidal metasurface with varing α values. (i) Measured THG power dependence for the metasurface (black squares, slope = 2.904) and a c-Si thin film of equal thickness (blue circles, slope = 3.064). (a)–(c) Reproduced from [136]. CC BY 4.0. (d)–(f) Reprinted with permission from [116]. Copyright (2019) American Chemical Society. (g)–(i) Reprinted with permission from [150]. Copyright (2024) American Chemical Society.

as clearly evidenced in the figure 6(f), shows that the THG enhancement is strongly influenced by α, and the highest TH intensity is observed at an intermediate asymmetry parameter of $\alpha = 0.175$, which is 10^{-6} under a pump power of 2.6 GW cm^{-2}. This result not only highlights the importance of Q_{rad} engineering, but also establishes a practical design guideline for achieving critical coupling in nonlinear metasurfaces.

Studies mentioned above primarily employ metasurfaces with geometrically symmetry-broken meta-atoms, which makes them exhibit polarization-dependent responses. While this polarization sensitivity offers advantages for applications such as polarization-selective switching or filtering, it often limits its performance in nonlinearity. To address this limitation, Liu *et al* [128]. demonstrated polarization-independent THG in Si metasurfaces by leveraging doubly degenerate quasi-BICs. The proposed metasurface design features a diatomic unit cell composed of two Si nanodisks with unequal radii arranged in a square lattice, which breaks translation symmetry while preserving C_{4v} rotational symmetry. Based on the numerical design, the authors fabricated a series of asymmetry metasurfaces with one nanodisk having varying radiis, and as the values of these two radiis approaching, an increasing Q factor is observed which reveals the existence of quasi-BICs. Besides, the reflectance spectra maintained consistent resonance positions and linewidths under different polarization angles, confirming the linear polarization-independent nature of the design. The high Q factor and strong field confinement facilitate the efficient nonlinear frequency conversion from the near-IR to visible light, achieving a maximum conversion efficiency of 1.03×10^{-5} at a pump intensity of 5.85 GW cm^{-2} with stable performance maintained under different polarization conditions. This work demonstrates that through the

disruption of translation symmetry while preserving C_{4v} rotational symmetry can produce quasi-BICs with polarization-independent responses for both linear and nonlinear optical responses, providing a valuable design principle for developing robust nonlinear photonic devices.

The above-described studies have successfully demonstrated enhanced THG in the near-IR to visible spectral range. To extend such efficient nonlinear frequency conversion to DUV regime, Abdelraouf *et al* [150]. utilized the interband plasmonic properties of the c-Si in the DUV, to fabricate a c-Si metasurface on a sapphire substrate for THG in the deep DUV regime. The designed meta-atom comprises two mirrored right-angle trapezoidal c-Si pillars. Structural symmetry breaking was achieved through a length difference (ΔL) between the top (L_1) and bottom (L_2) edges of the trapezoidal pillars, as illustrated in figure 6(g), and the degree of asymmetry is quantified by the parameter $\alpha = \Delta L/L_2$. This design enables high-Q factor BIC resonances. Experiments conducted revealed that the increasing α induces both a blue shift and broadening of the BIC resonance linewidth while reducing the Q factor as shown in figure 6(h). This effect originates from the modified coupling between EQ and MQ modes at shorter wavelengths. Power dependence of THG from this mirrored-trapezoidal metasurface is plotted in figure 6(i), and at an asymmetry parameter of $\alpha = 0.22$, the system achieved maximum THG conversion efficiency 5.2×10^{-8} under 15.5 GW cm^{-2} pump power. Notably, this result represents a 14-fold improvement over previously reported dielectric metasurfaces operating under comparable conditions in the DUV, marking a significant advance towards compact and efficient ultraviolet (UV) light sources.

In addition to enhancing nonlinear conversion efficiency, Si metasurfaces can also serve as multifunctional platforms for nonlinear signal modulation. As demonstrated in work by Xu *et al* [151], by combining the advantages of Mie resonators and BICs, they designed an ultrathin resonant Si disk metasurface. The introduction of off-centered holes in each nanodisk breaks the C_2 symmetry, opening a radiation channel of the BICs in the system. With the offset value increasing, a clear decrease of Q factor can be observed, confirming the formation of quasi-BICs. Multipolar decomposition analysis demonstrates that these states are dominated by MD response, yielding a forward third-harmonic conversion efficiency of approximately 10^{-5} at a peak pump intensity of 1.0 GW cm^{-2}. These high-Q MD quasi-BIC states enable efficient dynamic control of nonlinear emissions. Therefore, for a further application, the researchers implemented two distinct image-switching mechanisms: polarization-dependent control through orthogonally oriented nanodisk arrays (encoding↑and↓patterns), and wavelength-selective switching using spectrally tuned resonators (1325 nm and 1355 nm MD quasi-BIC states). This approach enables dynamic control over nonlinear image readout, establishing a compact and reconfigurable platform for functional nonlinear nanophotonic devices.

In this section, recent advances in Si metasurfaces have demonstrated efficient THG from near-IR to visible and even DUV wavelengths, also enable dynamic image switching through wavefront control. Although the inherently lower conversion efficiency of THG compared to SHG restricts its practical applications, ongoing efforts continue to explore its potential. Beyond existing studies about THG in metasurfaces, future progress may arise from alternative material platforms and novel physical mechanisms. Exploring new nonlinear materials presents a promising avenue for improving THG efficiency in metasurfaces. For instance, BP has high nonlinear susceptibility ($\sim$30pm V^{-1}) and its lattice orientation can be designed to align with the polarization direction of quasi-BIC modes to maximize the nonlinear coupling efficiency. Moreover, TiO_2 can be used for THG in visible and UV regime, while As_2S_3 is demonstrated the possibility of THG in the mid-IR by Gao *et al* [152]. which is enabled by phase-locking between the fundamental and harmonic waves. The further advances in THG metasurfaces will likely arise not only from the continued refinement of structural designs, but also from the integration of unconventional materials and the exploitation of novel nonlinear interactions. Future improvements will likely come from the integration of such emerging materials with advanced quasi-BIC designs, opening new avenues for THG-based nanophotonic applications.

5. Other effects

5.1. Nonlinear chirality effects

While the preceding sections on SHG and THG have primarily focused on enhancing nonlinear conversion efficiency through high-Q quasi-BIC resonances, another powerful strategy for advancing nonlinear metasurface functionality lies in controlling the polarization state of the generated light. By breaking mirror symmetry, asymmetry metasurfaces can be designed to support circularly polarized modes, enabling spin-dependent light–matter interactions and giving rise to nonlinear chiral effects. Such effects, including enhanced nonlinear circular dichroism (CD) which refers to the different nonlinear optical response under left- and right-handed circularly polarized excitation $CD^n = (I^n_R - I^n_L)/(I^n_R + I^n_L)$ where n is the order of harmonics generation. This not only expands the application scope of asymmetry

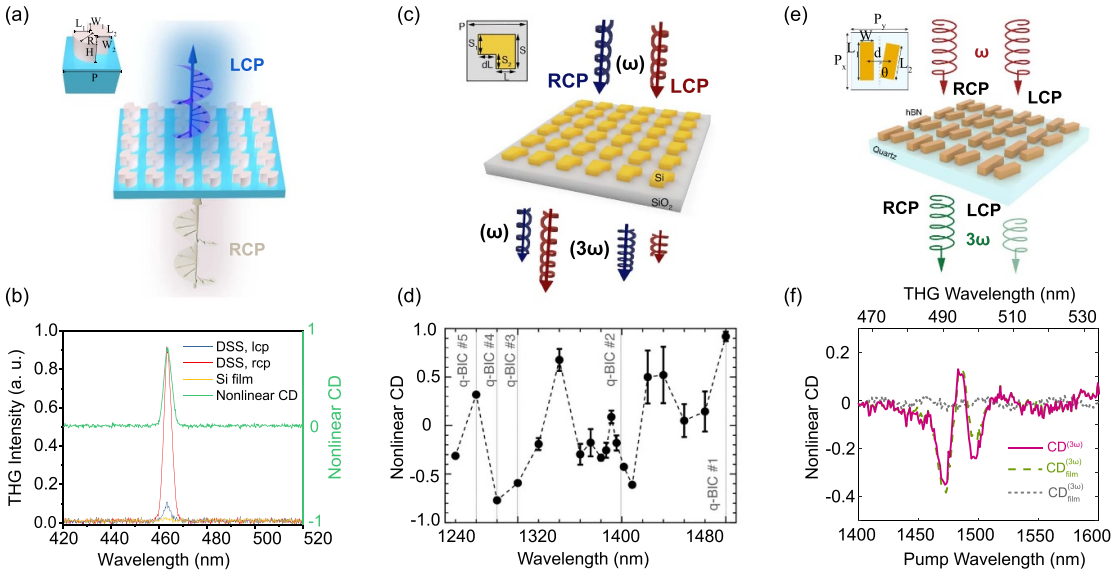


Figure 7. Nonlinear asymmetry metasurfaces for THG. (a), (b) Shi's realization of nonlinear CD in a double-sided scythe (DSS) shaped Si metasurface: (a) Illustration of planar chiral quasi-BIC metasurfaces comprising unit cell formed by the α-Si DSS structures on a SiO2 substrate, exhibiting 2D chirality for circular dichroism in transmission. (b) Measured THG intensities under right-handed polarization (RCP), left-handed polarization (LCP) incidences in the DSS-shaped metasurface, and in a reference Si thin film, as well as the nonlinear CD spectra. (c), (d) Koshelev's demonstration of nonlinear chiroptical response from a L-shaped Si metasurface: (c) Schematic of the Si metasurface with with broken-symmetry L-shaped meta-atoms and its linear and nonlinear characteristics (d) Measured nonlinear CD spectrum from the asymmetry L-shaped Si metasurface, showing a tunable range from -0.771 to $+0.918$. (e), (f) Tonkaev's work reporting a strong CD from a non-parallel-bars hBN metasurface: (e) Schematic image of the hBN chiral nonlinear metasurfaces showing a nonlinear chiroptical response, comsisting of a square lattice of non-parallel asymmetric nanobar dimers. (f) Spectrum of nonlinear CD for full signal (green), copolarized excitation and collection (pink) from the non-parallel-bar hBN metasurface, and nonlinear CD from a reference unpatterned film (gray). (a), (b) Reproduced from [154]. CC BY 4.0. (c), (d) Reprinted with permission from [119]. Copyright (2023) American Chemical Society. (e), (f) Reprinted with permission from [155]. Copyright (2024) American Chemical Society.

metasurfaces beyond efficiency enhancement, but also provide new opportunities for quantum photonics, and chiral sensing [58] . The first theoretical proposal for leveraging quasi-BICs to enhance nonlinear CD in asymmetry metasurfaces was proposed by Gandolfi *et al* [153]. In this work, the authors investigated a Si metasurface composed of asymmetric dielectric dimers arranged on a glass substrate, supporting high-Q quasi-BIC modes in the near-IR spectral range.

The pioneering experimental observations by Shi *et al* [154] demonstrated how the breaking c_z^2 symmetry in BIC-based metasurfaces gives rise to off-Γ C-points, which manifest extrinsic chirality under oblique illumination or via structural perturbations. This work suggests a design of chiral metasurface by employing double-sided scythe (DSS) shaped a-Si (α-Si) nanostructures with breaking c_z^2 symmetry to construct the BIC state. The unit cell of the planar metasurface can be described by a set of parameters: P, R, L_1, L_2, W_1, W_2, and H as depicted in figure 7(a). Such engineered BIC state exhibit strong birefringent properties that supports a vortex polarization singularity (V-point) enveloped by elliptical eigenstates with non-zero helicity, providing a convenient way to achieve high-Q chirality by slightly perturbing the inversion symmetry. Through illumination symmetry breaking, the BIC state undergoes transformation into a quasi-BIC, exhibiting strong extrinsic chirality with precisely tunable spectral linewidth. Alternatively, the introduction of in-plane structural asymmetries ($L_1 \neq L_2$) facilitates the emergence of intrinsic planar chirality at normal incidence. Figure 7(b) shows the measured THG intensity under right-handed polarization (RCP) and left-handed polarization (LCP) incidence, yielding ultra-high nonlinear CD of 0.81. Beyond the chirality based on circular polarization, the authors also envision the elliptical chirality by varying simultaneously birefringence and axis angle of the meta-atoms. This metasurface platform thus enables simultaneous control over both linear and nonlinear chiral optical responses, offering versatile functionality for advanced spin-selective photonic applications.

Building upon this experimental foundation, Koshelev *et al* [119]. provided a more detailed investigation of the interplay among symmetry perturbations, quasi-BIC resonances, and nonlinear chirality. In this study, they fabricated Si metasurfaces comprising L-shaped meta-atoms (figure 7(c)) designed to support resonant quasi-BIC modes in the near-IR wavelength range (1240 to 1500 nm). They firstly confirmed the linear CD reaching up to 0.3 at the quasi-BIC resonances originating from the interaction of modes with the substrate. Furthermore, by regulating the geometric symmetry perturbation

parameter (ΔL), they revealed that certain quasi-BIC modes exhibit significantly enhanced local fields and nonlinear polarization, surpassing other quasi-BIC resonances by several orders of magnitude. This enhancement was found to be closely linked to the approaching to critical coupling conditions in equation (12). Importantly, the nonlinear CD could be continuously tuned across a wide range while maintaining high THG efficiency. In particular, the nonlinear CD for design of $\Delta L = 300$ nm was experimentally varied from $+0.918 \pm 0.049$ to -0.771 ± 0.004 as shown in figure 7(d), demonstrating precise helicity control over nonlinear light emission in asymmetry metasurfaces.

Beyond conventional dielectric materials like Si, the integration of van der Waals crystals offers new opportunities for enhancing nonlinear chiral responses in asymmetry metasurfaces. The nonlinear hBN metasurface developed by Tonkaev *et al* [155] comprises a square lattice of non-parallel nanobar dimers as depicted in figure 7(e), with geometrical parameters are $L_1 = 864$ nm, $L_2 = 744$ nm, $W = 240$ nm, $d = P_y/2 = 538$ nm, $P_x = 1025$ nm, $P_y = 1075$ nm, on fused Si. The length reduction and angular offset of one nanobar lead to quasi-BIC resonances in near-IR range (1400 to 1600 nm) and structural chirality. Through numerical calculations, the linear CD is around +0.01 at the resonance. Besides, experimental results demonstrate resonant nonlinear responses, with quasi-BIC-enhanced THG showing a 10^3-fold intensity increase, with a conversion efficiency of 10^{-6} at a peak intensity of 10 GW cm^{-2}. And tunable nonlinear CD ranging from −0.38 to +0.12 (figure 7(f)), while concurrent SHG exhibits a nonlinear CD of −0.27. This study introduces a new material platform for chiral photonics, which can be employed for chiral biosensing in the whole visible and near-UV frequency ranges.

Taken together, these studies highlight the rapid progress in leveraging asymmetry metasurfaces for controlling the polarization state of nonlinear emissions, enabling functionalities such as tunable nonlinear CD, spin-selective light generation, and multi-resonant chiral responses [156–159]. These advances illustrate that, beyond merely enhancing frequency-conversion efficiency, structural symmetry engineering in asymmetry metasurfaces can further unlock additional degrees of freedom in nonlinear light control. While these chiral effects focus on tailoring the spin and polarization properties of the generated light, another compelling direction for expanding the capabilities of asymmetry metasurfaces lies in pushing the frequency of the generated photons to much higher harmonic orders. Such HHG processes demand extreme field confinement and precise modal control–features that asymmetry metasurfaces are uniquely positioned to provide.

5.2. High-harmonic generation

Building upon the quasi-BIC-enabled enhancement strategies discussed earlier for SHG, THG, and nonlinear chirality, HHG represents the next step in extending nonlinear optical processes to the extreme UV and beyond. HHG process involves the nonlinear upconversion of incident photons, leading to the emission of photons with frequencies exceeding three times that of the fundamental field. Traditionally, HHG has been associated with extreme nonlinear regimes requiring ultrahigh intensities and long interaction lengths, typically realized in atomic gases or bulk crystals. Like relevant researches in THG, Si is also widely applied in HHG applications. The first article on HHG in Si metasurfaces, authored by Liu *et al* [160], reported the measurement of odd harmonics up to the 11th order. Recent theoretical and experimental studies have demonstrated that the strong field confinement and precise phase matching enabled by quasi-BIC resonances facilitate efficient HHG at lower input power thresholds.

Following the initial demonstration, Zograf *et al* [118] brought the concept of BICs to the field of HHG by employing asymmetry metasurfaces to generate efficiently high optical harmonics. In this paper, they carried out a design of asymmetry metasurfaces comprising complex meta-atoms in the form of an asymmetric pair of rectangular Si bars on a sapphire substrate as shown in figure 8(a). The two bars in each pair have the widths w and $w - dw$, respectively, and the asymmetry parameter is defined as $\alpha = dw/w$. This geometric asymmetry influenced the loss characteristics of quasi-BICs, with optimal field enhancement occurring at $\alpha = 0.2$ under critical coupling conditions in equation (12), which is important for the observation of high-order harmonics. Through conducting experiments, they observed a distinct transition to the nonlinear regime for harmonics up to the 11th order with enhanced generation efficiency at specific pump wavelengths and polarization states (figure 8(b)). While even-order harmonics are typically forbidden in centrosymmetric media, surface effects and symmetry breaking in the metasurface design can enable their emergence. To further explain the mechanism in this asymmetry metasurface discussed above, a later work by Tonkaev [163] used a same metasurface design, and demonstrated optical harmonics up to fourth order generated under the normal incidence driven by BICs and guided-mode resonances.

The HHG in above asymmetry metasurfaces are fundamentally constrained to a narrow spectral range near one or a few resonant frequencies. To overcome this limitation, Jangid *et al* [161] proposed

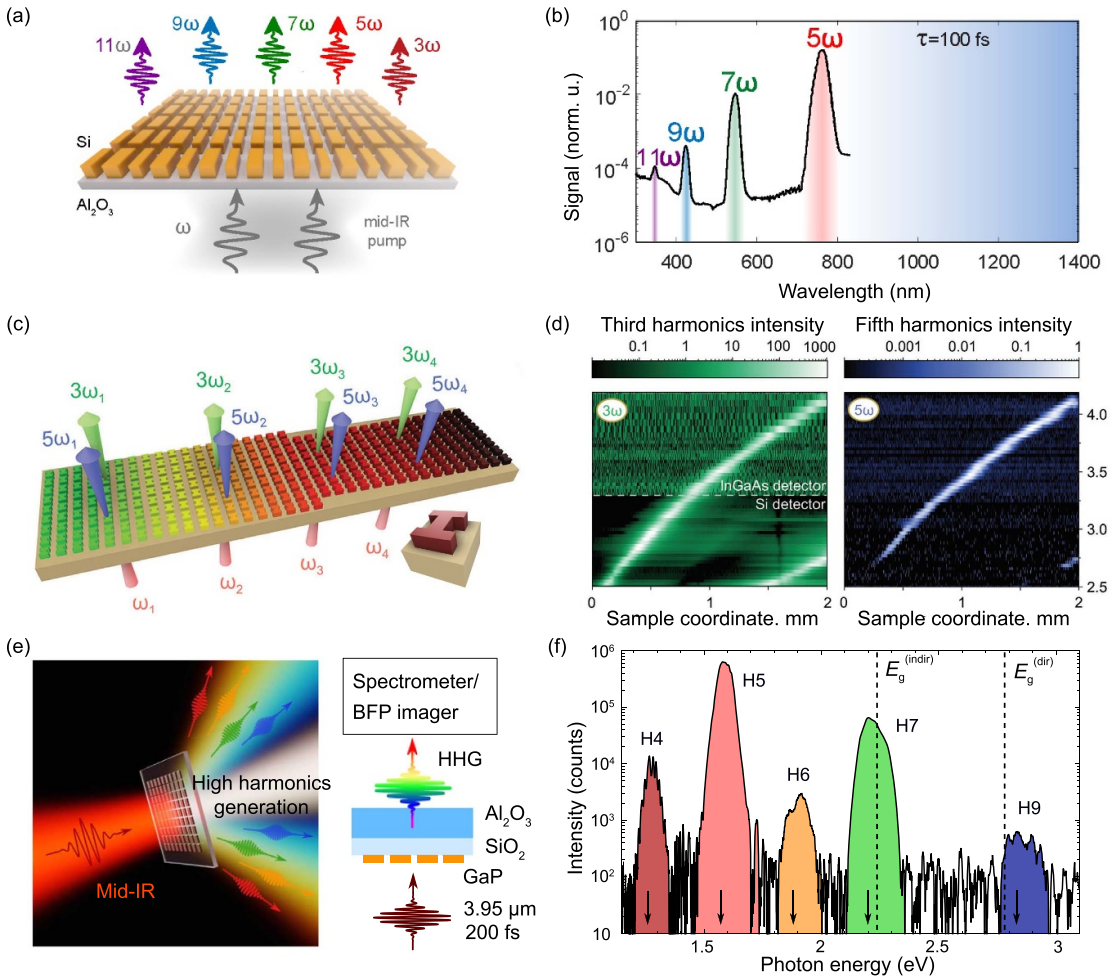


Figure 8. Examples of enhanced HHG in Nonlinear asymmetry metasurfaces. (a), (b) Zograf's demonstration of HHG in a two-bar Si metasurface: (a) Conceptual diagram of 3rd to 11th optical harmonics generation from the two-bar metasurface. Metasurface is pumped by a focused mid-IR laser beam and generate harmonics in near-IR and visible range. (b) Spectrum of HHG from the two-bar metasurface by 100 fs laser pulses. (c), (d) Jangid's realization of spectrally tunable HHG in a bone-like resonance-gradient metasurface: (c) Illustration of the bone-like metasurface, showing that varying wavelength exciting with a pulsed laser in mid-IR range at varying lateral coordinates of the metasurface can produce enhanced and tunable generation of the third and fifth harmonics in near-IR and visible range. (d) Continuous spectral tuning of 3rd and 5th harmonic generation from the bone-like metasurface. (e), (f) Shcherbakov's realization of HHG in a GaP metasurface: (e) Concept diagram of the HHG process in the GaP metasurfaces. Visible high harmonics emit from the metasurfaces driven by a mid-IR pump, the odd harmonics are observed co-polarized with the pump while the even harmonics are elliptically polarized. (f) 4th to 9th order harmonics generation spectrum from the GaP metasurface, 8th harmonic is not observed due to the onset of indirect interband transitions in GaP. (a), (b) Reprinted with permission from [118]. Copyright (2022) American Chemical Society. (c), (d) [161] John Wiley & Sons. © 2023 Wiley-VCH GmbH. (e), (f) Reproduced from [162]. CC BY 4.0.

a novel approach involving resonance-gradient metasurfaces with varying geometric parameters, which induces a coordinate-dependent shift in resonant frequencies. As illustrated in figure 8(c), the metasurface consists of a series of bone-shaped Ge resonators fabricated on a calcium fluoride (CaF_2) substrate. Compared with Si, Ge possesses a higher $\chi^{(3)}$ and refractive index in mid-IR region, enabling stronger field confinement and highly efficient HHG. Its compatibility with state-of-the-art large-scale-fabrication methods further meet the precise requirements for manufacturing gradient metasurfaces. To enable tunable harmonics generation, this design was proportionally scaled by factors ranging from 0.8 to 2, to match the tuning range of the main mode of the bone-like Ge resonator with the available spectral bandwidth of the tunable laser. Critically, the metasurface's parameter gradient was carefully optimized to be sufficiently gradual, such that the localized laser excitation at any given position. Based on such asymmetry metasurfaces, the researchers demonstrated spectrally tunable and resonantly enhanced third- and fifth-harmonic generation by systematically varying the excitation spot position in accord with the laser wavelength (figure 8(d)). This approach achieves broadband resonant enhancement of tunable HHG within a single metasurface, offering new possibilities for diverse nanophotonic designs and material platforms.

Moreover, beyond individual demonstrations of either even- or odd-order HHG, Shcherbakov *et al* [162]. have demonstrated their simultaneous generation using an ultrathin GaP metasurface platform

driven by intense mid-IR laser pulses (figure 8(e)). The metasurface comprises densely packed domino-shaped dielectric resonant antennas that support ED modes at a nominal resonant wavelength of $\lambda_{res}^{(0)} = 3.95\,\mu$m. The non-centrosymmetric zincblende crystal structure, wide bandgap, high refractive index, and mid-IR transparency of GaP collectively enable efficient generation of both even- and odd-order harmonics across 1.3–3 eV photon energies while minimizing reabsorption losses and enhancing nonlinear effects through strong electromagnetic field localization in the metasurface. Driven by the femtosecond pulse, visible high harmonics from 4th order to 9th order emit from the metasurfaces as shown in figure 8(f), while the conversion efficiency of the seventh harmonic reaches a value of $\sim 2\times10^{-9}$ at pump intensity of 80 GW cm^{-2}. Notably, the observed lower efficiency of even-order harmonics is attributed to suboptimal alignment of the GaP crystal axes within the antennas. This work establishes a practical platform for investigating parity-mixed harmonic generation in solid-state nanophotonics, paving a new avenue for ultracompact light sources across a broad spectral range.

Apart from the materials already mentioned, $LiNbO_3$ is also a material that has drawn great interest in nonlinear optics because of its large second-order nonlinear susceptibility and broad optical transparency. Recent work by Zhao *et al* [164] demonstrated the implementation of a $LiNbO_3$ metasurface with guided-mode resonances can be used to achieve a SHG efficiency of 8.6×10^{-3} at peak pump power intensity of 170 GW cm^{-2} and HHG up to the 7th order in the DUV spectral region. Additionally, in metasurface-enhanced HHG, a wide range of materials with potential applications still remain unexplored, offering opportunities for improved functionality and higher conversion efficiency. Altogether, these studies suggest that future advances in HHG-enabled asymmetry metasurfaces may emerge from new architectural concepts such as spatial resonance engineering, and from the exploration of novel material platforms beyond the conventional semiconductors, enabling expanded functionality, higher conversion efficiency, and broader spectral tunability in compact nonlinear photonic systems.

5.3. Photon pair generation

In addition to harmonics generation processes such as SHG, THG and HHG, SPDC represents another fundamental nonlinear optical process. SPDC is a second-order nonlinear optical process in which a single pump photon is spontaneously converted into two lower-energy photons, satisfying both energy and momentum conservation. When these photons exhibit quantum correlations in degrees of freedom such as polarization, momentum or energy, they form an entangled photon pair [165–169]. The coincidence rate and the coincidence-to-accidental ratio (CAR) serve as two key metrics for evaluating the performance of photon pair sources. The coincidence rate quantifies the generation rate of photon pairs, representing the brightness or yield of the source, while CAR characterizes the ratio of true correlated events to accidental coincidences, reflecting the purity and signal-to-noise quality of the generated quantum correlations. This property makes SPDC a cornerstone technique in quantum optics, particularly for the generation of entangled photon pairs [170]. Recent advance by Santiago-Cruz [132] has demonstrated that asymmetry metasurfaces based on highly nonlinear materials can significantly enhance SPDC efficiency by relaxing traditional phase-matching constraints and leveraging resonant field enhancement as illustrated in figure 9(a). Due to high-Q resonances and mode overlap control, these systems enable efficient generation of entangled photon pairs with tunable polarization states and frequency correlations. significant two-photon coincidence counts are observed as shown in figure 9(b), confirming the high efficiency of photon pair generation. Meanwhile, the fundamental properties of both ED and MD resonances from quasi-BICs are preserved, with Q factors reaching $\sim$330 and $\sim$1000, respectively.

To investigate multiplexed entangled photon generation via this quantum optical metasurfaces (QOMs) design, the researchers fabricated three distinct QOMs (QOM-A, QOM-B, and QOM-C) with different resonator sizes and spacings, thereby tuning the ED and MD quasi-BIC optical modes to different resonant wavelengths. In QOM-A, pumping at 723.4 nm resulted in degenerate photon the pair emission at $2\lambda_p = 1446.8$ nm, with a single narrow peak overlapping with the ED quasi-BIC resonance in the spectrum shown in figure 9(c). For QOM-B, when the pump wavelength was off-resonance from the ED quasi-BIC resonance, the SPDC spectrum in figure 9(d) revealed two narrow peaks, corresponding to non-degenerate biphoton emission with one photon ω_s appearing at the resonance wavelength, and the conjugate photon ω_s at the wavelength defined by the energy conservation law: $\omega_i = \omega_p - \omega_s$. More interestingly, when pumping QOM-C at 725.4 nm, with 175° polarized radiation, the MD quasi-BIC resonance can be activated. This multi-resonant configuration enables simultaneous excitation of multiple SPDC processes, resulting in a more complex emission spectrum with four peaks. As evident in figure 9(e), this spectrum reveals two pairs of non-degenerate entangled photons, with signal photons emitted at the ED quasi-BIC (1359.4 nm) and MD quasi-BIC (1429.4 nm) resonances, along with their respective idler partners. Based on these studied QOMs, they proved that these asymmetry metasurfaces

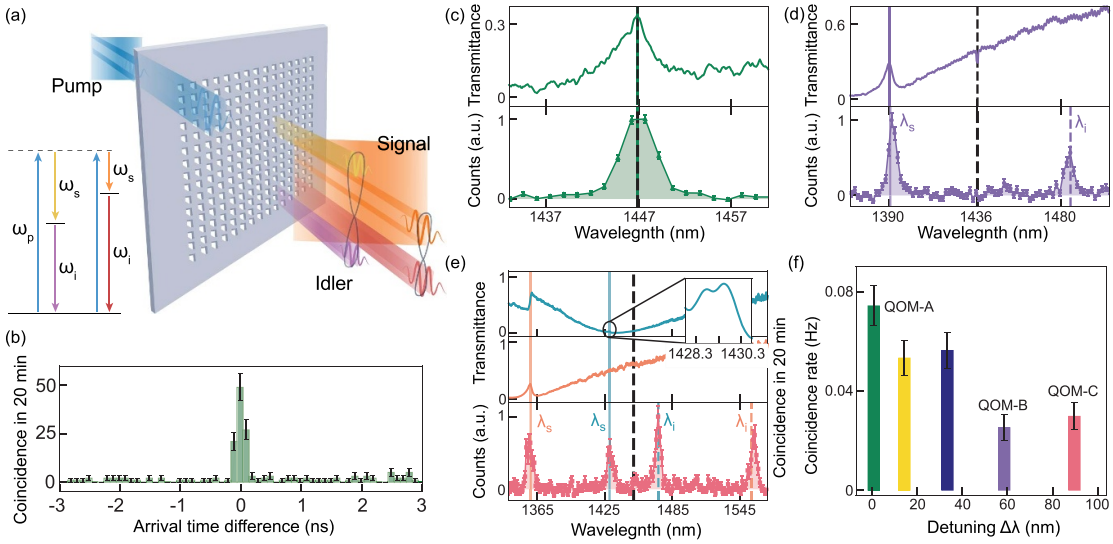


Figure 9. SPDC using symmetry-protected quasi-BICs in a L-shaped metasurface. (a) Concept diagram of multiplexed entangled photon generation in the L-shaped semiconductor metasurface. Metasurfaces is pumped with linearly polarized CW, and generate photon pairs. The experimental results below are based on the metasurface shown in (a). (b) Typical distribution of the photon arrival time difference for two detectors, indicating the presence of photon pairs from the metasurface. (c)–(e) Show measured transmission spectra (top) and SPDC spectra (bottom) for three QOMs, QOM-A, QOM-B and QOM-C: (c) QOM-A generating degenerate photon pairs at wavelength $2\lambda_p = 1446.8$ nm. (d) QOM-B generating nondegenerate photon pairs with signal photon is emitted at $\lambda = 1390.9$ nm. (e) QOM-C generating two types of nondegenerate photon pairs, where two signal photons are emitted at $\lambda = 1359.4$ nm and at $\lambda = 1429.4$ nm respectively. (f) Coincidence rate versus wavelength detuning $\Delta\lambda = 2\lambda_p - \lambda_{(ED)}$ ($\lambda_{(ED)}$ is the wavelength of quasi-BIC resonance) of five different QOMs. Error bars denote the statistical uncertainty. From [132]. Reprinted with permission from AAAS.

can produce degenerate and nondegenerate photon pairs across a broad spectral range while maintaining high coincidence rate (figure 9(f)). Especially for QOM-A, this configuration has the highest rate ~868 pairs $s^{-1}W^{-2}$. Furthermore, by adding multiple coherent pump beams at different wavelengths, and matching the pump wavelength separation and the optical resonances of the QOM, photons at multiple wavelengths can be entangled via pairwise coupling. This opens the door for scalable generation of entangled cluster states, a critical resource for implementing one-way quantum computation on integrated photonic platforms.

Expect for spectral entanglement, spatial or angular entanglement also plays a crucial role in quantum applications, such as quantum communication and quantum imaging. In this context, Zhang *et al* [165]. demonstrated the ability of nonlinear metasurfaces to generate spatially entangled photon pairs through SPDC in a $LiNbO_3$ metasurface covered by a silica meta-grating. Their results showed the metasurface enhanced SPDC efficiency by approximately 450 times compared to unpatterned films, while achieving a CAR of around 5000 and a coincidence rate ~249 pairs $s^{-1}W^{-2}$, representing a an order of magnitude higher then previous works. Spatial correlation measurements further confirmed the nonclassical correlations between photons emitted from different spatial modes, verifying their entangled nature. Another emerging material platform for SPDC is AlGaAs, valued for its strong second-order nonlinearity. Mazzanti *et al* [171] demonstrated angle correlated photon pairs using a metasurface consisted of an AlGaAs grating on a glass substrate.

The field of nonlinear quantum metasurfaces is rapidly emerging, and its future developments are expected to explore several promising directions. One major avenue for progress lies in the investigation of alternative material platforms. While current researches primarily focus on nonlinear semiconductors, the inclusion of 2D materials can open up new opportunities for controlling quantum properties at the nanoscale [172–174]. Furthermore, more sophisticated structural designs will likely be developed to support topological states, which may enable robust confinement and propagation of quantum states in QOMs. In addition, the integration of additional photonic degrees of freedom, such as polarization states [175] and orbital angular momentum modes, will provide the necessary tools for multidimensional quantum state engineering and high-dimensional quantum information processing. These combined advancements will likely enhance the versatility of metasurfaces, enabling novel applications in quantum communication, sensing, and computation that extend beyond current technological limits.

Table 3. Summary of the conversion efficiency of different structures.

Process	Structures	Efficiency	Pump ($GW\,cm^{-2}$)	Coincience Rate ($pairs\,s^{-1}\,W^{-2}$)
SHG	GaAs L-shaped pillar [126]	6×10^{-5}	3.1	
	GaP tilted-elliptical eylinders [142]	2×10^{-7}	1×10^{-6}	
	$LiNbO_3$ thin film [146]	10^{-6}	4.3	
THG	Si T-shaped pillar [136]	10^{-6}	0.1	
	Two-bar Si metasurface [116]	10^{-6}	2.6	
	Si metasurface with hybridization of two lattices [128]	1.03×10^{-5}	5.85	
	Mirrored-trapezoidal c-Si metasurface [150]	5.2×10^{-8}	15.5	
	Si disk metasurface [151]	10^{-5}	1.0	
	Non-parallel-bars hBN metasurface [155]	10^{-6}	10	
HHG	GaP metasurface [162]	2×10^{-9}[a]	80	
SPDC	GaAs L-shaped pillar [132]			868
	Silica meta-grating [165]			249

[a] Conversion efficiency of seventh order harmonics.

6. Conclusion

This review has provided a comprehensive overview of recent advances in asymmetry metasurfaces, with particular focus on their enhancement effects in nonlinear applications. Relevant nonlinear efficiencies are listed in table 3. Beyond these processes, asymmetry metasurfaces have also shown potential for SFG and FWM under dual-pump configurations [176, 177]. Fundamentally, the enhancement of nonlinear effects in asymmetry metasurfaces arises from their unique structural design, which enables the excitation of quasi-BICs. These high-Q resonances dramatically confine local electromagnetic field, thereby boosting nonlinear conversion efficiencies. In addition, material selection also plays an important role in optimizing nonlinear performance. Employing materials with high nonlinear susceptibility can directly improve conversion efficiency. Further improvements can be achieved through advanced fabrication techniques or by incorporating novel mechanisms, such as the integration of 2D materials with asymmetry metasurfaces, offering additional degrees of freedom for engineering nonlinear responses and paving the way towards multifunctional, highly efficient, and compact photonic platforms.

Despite extensive research efforts devoted to optimizing asymmetry metasurface designs for higher Q factors, the Q factors of symmetry breaking induced quasi-BICs in current experiments generally remain limited to around 10 000, substantially lower than those achieved by microring or microdisk resonators. This limitations arises from fundamental constraints in both material properties and fabrication precision. On one hand, intrinsic material limitations, particularly optical absorption losses and finite nonlinear susceptibilities impose boundaries on device performance. On the other hand, the precise control of structural asymmetry faces implementation hurdles due to the exacting demands of nanoscale fabrication tolerances. These persistent challenges continue to motivate extensive research efforts into the field of high-Q asymmetry metasurface designs. Based on the current state of the field, we suggest several directions for researchers to explore solutions.

First, asymmetry metasurfaces with high refractive index can enable stronger light-field localization, effectively suppressing radiative losses which is a critical factor for achieving high-Q resonances. As mentioned recently [178], increasing the refractive index by a modest factor with modern methods of growth, fabrication, and subwavelength patterning can significantly boost the Q factor of asymmetry metasurfaces. Another promising approach is to employ high-index materials to construct asymmetry metasurfaces that can still support optical modes. For example, TMD-based metasurfaces have been shown to support BICs, enabling high-Q modes in the visible and parts of the IR spectrum. However, despite its high-index characteristics, research progress in this area still remains limited with only a handful of studies reported to date [179]. The main challenge lies in the fabrication of few-layer TMD metasurfaces, as such 2D materials with extreme thickness demand highly precise fabrication to realize

necessary structural control. Further advancements in this emerging field are expected to overcome these challenges and yield novel insights into the design and applications of TMD-based metasurfaces.

Second, exploring new schemes to regulate the quasi-BICs to achieve higher Q factor provides another perspective on the solution. Novel designs of asymmetry metasurfaces provide new opportunities to excite quasi-BICs with higher Q factors. In contrast to traditional symmetry breaking method used to form symmetry-protected quasi-BICs, recent research proposes a more precisely controlled asymmetric design, achieved through angular perturbation engineering [138] . This technique enables accurate tuning of structural asymmetry while maintaining both high Q factor precision and excellent reproducibility, thereby establishing a new design paradigm for high-Q asymmetry metasurfaces. In addition, most BICs reported so far correspond to low-order multipolar BICs, such as MD BICs and TD BICs. Future research could explore higher-order multipolar BICs, which offer greater flexibility in tailoring far-field scattering properties. Finally, although quasi-BICs have also been demonstrated in individual dielectric nanoparticles, their Q factors remain moderate. It is reasonable to expect that engineering coupling effects among multiple dielectric nanoparticles could further boost Q factors.

Third, artificial intelligence (AI) offers a powerful route for optimizing asymmetric metasurfaces [180, 181]. The high design freedom in asymmetry metasurfaces for nonlinear applications makes them particularly suitable for optimization through advanced computational methods. By employing AI-assisted parameter optimization and structural layout refinement, researchers can systematically achieve target nonlinear efficiencies in metasurface designs. Among various AI tools, machine learning has become one of the dominant approaches in AI to solve complex data-driven problems which can be employed in asymmetry metasurfaces as a powerful way to obtain mapping between the topology and their associated functional features. Well-trained neural networks can further facilitate inverse design processes, effectively bypassing the need for computationally intensive electromagnetic simulations [182]. With the rapid development of AI, the on-demand design of asymmetry metasurfaces is foreseeable in the near future.

Through the above solutions ranging from material innovation and novel quasi-BICs engineering schemes to AI- assisted design, it is possible to significantly advance the performance of asymmetry metasurfaces in nonlinear applications. By employing these approaches, the conversion efficiency of asymmetry metasurfaces could potentially be enhanced to the order of 10^{-1} under a pump intensity of 10^{-3} GW cm^{-2}, reaching a level comparable to that achieved in periodically poled lithium niobate. Moreover, the operational spectral range can be extended to DUV, even extreme UV range, enabling broader nonlinear optical responses. Additionally, integrating multiple nonlinear mixing mechanisms within a single platform or coupling the metasurface with optical microcavities can provide additional flexibility for wavefront control and enhanced field confinement [183]. These advances open promising avenues for practical engineering applications. In particular, quasi-BICs in asymmetry metasurfaces hold strong potential for integrated laser systems, optical communication, quantum light generation, and nonlinear imaging. The combination of high efficiency, broadband operation, and on-chip integrability offers a viable pathway toward the next generation of ultracompact, multifunctional, and high-performance nonlinear photonic devices.

Acknowledgments

This research is supported by the National Natural Science Foundation of China (Grant Nos. 12574366, 12204019, 62035017), Guangdong Provincial Quantum Science Strategic Initiative (Grant Nos. GDZX2506005, GDZX2506001, GDZX2306003), and the National Super-Computer Center in Guangzhou.

Data availability statement

No new data were created or analysed in this study.

ORCID iDs

Zhuojun Liu 0000-0003-2063-8071
Bo Chen 0000-0002-5039-0663

References

[1] Cotter D, Manning R, Blow K, Ellis A, Kelly A, Nesset D, Phillips I, Poustie A and Rogers D 1999 *Science* **286** 1523–8
[2] Rashed A N Z, Mohammed A E N A, Zaky W F, Amiri I and Yupapin P 2019 *Results Phys.* **13** 102152

[3] Kravtsov V, Ulbricht R, Atkin J M and Raschke M B 2016 *Nat. Nanotechnol.* **11** 459–64
[4] Frischwasser K, Cohen K, Kher-Alden J, Dolev S, Tsesses S and Bartal G 2021 *Nat. Photon.* **15** 442–8
[5] Leach J, Jack B, Romero J, Jha A K, Yao A M, Franke-Arnold S, Ireland D G, Boyd R W, Barnett S M and Padgett M J 2010 *Science* **329** 662–5
[6] Howell J C, Bennink R S, Bentley S J and Boyd R W 2004 *Phys. Rev. Lett.* **92** 210403
[7] Krasnok A, Tymchenko M and Alù A 2018 *Mater. Today* **21** 8–21
[8] Huang T, Zhao X, Zeng S, Crunteanu A, Shum P P and Yu N 2020 *Rep. Prog. Phys.* **83** 126101
[9] Pertsch T and Kivshar Y 2020 *MRS Bull.* **45** 210–20
[10] Kang M, Liu T, Chan C and Xiao M 2023 *Nat. Rev. Phys.* **5** 659–78
[11] von Neumann J and Wigner E P 1993 Über merkwürdige diskrete eigenwerte *The Collected Works of Eugene Paul Wigner: Part A: The Scientific Papers* (Springer) pp 291–3
[12] Hsu C W, Zhen B, Stone A D, Joannopoulos J D and Soljačić M 2016 *Nat. Rev. Mater.* **1** 1–13
[13] Marinica D, Borisov A and Shabanov S 2008 *Phys. Rev. Lett.* **100** 183902
[14] Doeleman H M, Monticone F, den Hollander W, Alù A and Koenderink A F 2018 *Nat. Photon.* **12** 397–401
[15] Boyd R W, Gaeta A L and Giese E 2008 Nonlinear optics *Springer Handbook of Atomic, Molecular and Optical Physics* (Springer) pp 1097–110
[16] Plotnik Y, Peleg O, Dreisow F, Heinrich M, Nolte S, Szameit A and Segev M 2011 *Phys. Rev. Lett.* **107** 183901
[17] Savinov V, Fedotov V and Zheludev N I 2014 *Phys. Rev. B* **89** 205112
[18] Leuthold J, Koos C and Freude W 2010 *Nat. Photon.* **4** 535–44
[19] Shen Y R 2003 *The Principles of Nonlinear Optics* (Wiley) (available at: https://books.google.com.tw/books?id=xeg9AQAAIAAJ)
[20] Xu L *et al* 2019 *ACS Nano* **14** 1379–89
[21] Kruk S, Poddubny A, Smirnova D, Wang L, Slobozhanyuk A, Shorokhov A, Kravchenko I, Luther-Davies B and Kivshar Y 2019 *Nat. Nanotechnol.* **14** 126–30
[22] Löchner F J *et al* 2018 *ACS Photon.* **5** 1786–93
[23] Saerens G *et al* 2020 *Laser Photon. Rev.* **14** 2000028
[24] Sautter J D *et al* 2019 *Nano Lett.* **19** 3905–11
[25] Timofeeva M, Lang L, Timpu F, Renaut C, Bouravleuv A, Shtrom I, Cirlin G and Grange R 2018 *Nano Lett.* **18** 3695–702
[26] Camacho-Morales R *et al* 2019 *Nanoscale* **11** 1745–53
[27] Tu X, Feng S, Li J, Xing Y, Wu F, Liu T and Xiao S 2024 *Phys. Rev. A* **109** 063522
[28] Rocco D *et al* 2018 *Photon. Res.* **6** B6–B12
[29] Liu T, Qin M, Wu F and Xiao S 2023 *Phys. Rev. B* **107** 075441
[30] Camacho-Morales R *et al* 2016 *Nano Lett.* **16** 7191–7
[31] Kruk S S, Camacho-Morales R, Xu L, Rahmani M, Smirnova D A, Wang L, Tan H H, Jagadish C, Neshev D N and Kivshar Y S 2017 *Nano Lett.* **17** 3914–8
[32] Koshelev K, Kruk S, Melik-Gaykazyan E, Choi J H, Bogdanov A, Park H G and Kivshar Y 2020 *Science* **367** 288–92
[33] Carletti L *et al* 2018 *ACS Photon.* **5** 4386–92
[34] Marino G, Gigli C, Rocco D, Lemaître A, Favero I, De Angelis C and Leo G 2019 *ACS Photon.* **6** 1226–31
[35] Cambiasso J, Grinblat G, Li Y, Rakovich A, Cortés E and Maier S A 2017 *Nano Lett.* **17** 1219–25
[36] Khmelevskaia D *et al* 2021 *Appl. Phys. Lett.* **118** 201101
[37] Zheng Z, Xu L, Huang L, Smirnova D, Hong P, Ying C and Rahmani M 2022 *Phys. Rev. B* **106** 125411
[38] Wang J, Liu Z, Xiang J, Chen B, Wei Y, Liu W, Xu Y, Lan S and Liu J 2021 *Nanophotonics* **10** 4273–8
[39] Feng S, Liu T, Chen W, Wu F and Xiao S 2023 *Sci. China Phys. Mech.* **66** 124214
[40] Qu L, Bai L, Jin C, Liu Q, Wu W, Gao B, Li J, Cai W, Ren M and Xu J 2022 *Nano Lett.* **22** 9652–7
[41] Xu X, Trovatello C, Mooshammer F, Shao Y, Zhang S, Yao K, Basov D N, Cerullo G and Schuck P J 2022 *Nat. Photon.* **16** 698–706
[42] Tang Y *et al* 2024 *Nat. Commun.* **15** 9979
[43] Weissflog M A *et al* 2024 *Nat. Commun.* **15** 7600
[44] Trovatello C *et al* 2025 *Nat. Photon.* **19** 291–9
[45] Ling H, Tang Y, Tian X, Shafirin P, Hossain M, Vabishchevich P P, Harutyunyan H and Davoyan A R 2025 *Nano Lett.* **25** 9229–36
[46] Nauman M, Yan J, de Ceglia D, Rahmani M, Zangeneh Kamali K, De Angelis C, Miroshnichenko A E, Lu Y and Neshev D N 2021 *Nat. Commun.* **12** 5597
[47] Verre R, Baranov D G, Munkhbat B, Cuadra J, Käll M and Shegai T 2019 *Nat. Nanotechnol.* **14** 679–83
[48] Sung J, Shin D, Cho H, Lee S W, Park S, Kim Y D, Moon J S, Kim J H and Gong S H 2022 *Nat. Photon.* **16** 792–7
[49] Liu Z, Chen B, Wang X, Qiu G, Cao Q, Wei D and Liu J 2024 *Nanophotonics* **13** 4029–35
[50] Fang L, Yuan Q, Fang H, Gan X, Li J, Wang T, Zhao Q, Jie W and Zhao J 2018 *Adv. Opt. Mater.* **6** 1800698
[51] Gan X T, Zhao C Y, Hu S Q, Wang T, Song Y, Li J, Zhao Q H, Jie W Q and Zhao J L 2018 *Light Sci. Appl.* **7** 17126
[52] Li S, Zhou C, Liu T and Xiao S 2019 *Phys. Rev. A* **100** 063803
[53] Xiao S, Qin M, Duan J, Wu F and Liu T 2022 *Phys. Rev. B* **105** 195440
[54] Wang X, Liu Z, Chen B, Qiu G, Wei D and Liu J 2024 *Nano Lett.* **24** 11327–33
[55] Qin M, Wei G, Xu H, Ma R, Li H, Gao W, Liu J and Wu F 2024 *Appl. Phys. Lett.* **124** 051703
[56] Qin M, Wu F, Liu T, Zhang D and Xiao S 2025 *Phys. Rev. B* **111** 035414
[57] Zubyuk V V, Shafirin P A, Shcherbakov M R, Shvets G and Fedyanin A A 2022 *ACS Photon.* **9** 493–502
[58] Semmlinger M, Zhang M, Tseng M L, Huang T T, Yang J, Tsai D P, Nordlander P and Halas N J 2019 *Nano Lett.* **19** 8972–8
[59] Papatryfonos K *et al* 2021 *AIP Adv.* **11** 025327
[60] Fleming J W *et al* 2018 *Handbook of Optical Materials* (CRC Press)
[61] Shoji I, Kondo T, Kitamoto A, Shirane M and Ito R 1997 *J. Opt. Soc. Am. B* **14** 2268–94
[62] Vabishchevich P and Kivshar Y 2023 *Photon. Res.* **11** B50–B64
[63] Ohashi M, Kondo T, Ito R, Fukatsu S, Shiraki Y, Kumata K and Kano S 1993 *J. Appl. Phys.* **74** 596–601
[64] Jellison J G 1992 *Opt. Mater.* **1** 151–60
[65] Schunemann P, Pollak T, Yang Y, Teng Y Y and Wong C 1988 *J. Opt. Soc. Am. B* **5** 1702–10
[66] Wemple S 1970 *Phys. Rev. B* **2** 2679
[67] Zhang Y, Wu J, Yang Y, Qu Y, Jia L, Moein T, Jia B and Moss D J 2020 *ACS Appl. Mater. Interfaces* **12** 33094–103
[68] Nikogosyan D N 2005 *Nonlinear Optical Crystals: a Complete Survey* (Springer)
[69] Bergstrom L, Meurk A, Arwin H and Rowcliffe D J 1996 *J. Am. Ceram. Soc.* **79** 339–48

[70] Wang G, Wong G K and Ketterson J B 2001 *Appl. Opt.* **40** 5436–8
[71] Yan X, Tian T, Wang M, Shen H, Zhou D, Zhang Y and Xu J 2020 *Crystals* **10** 71
[72] Lopez-Rodrigue B *et al* 2023 *ACS Photonics* **10** 3748–54
[73] Niedermeier S, Schillinger H, Sauerbrey R, Adolph B and Bechstedt F 1999 *Appl. Phys. Lett.* **75** 618
[74] Munkhbat B, Wróbel P, Antosiewicz T J and Shegai T O 2022 *ACS Photon.* **9** 2398–407
[75] Rahman I A and Purqon A 2017 First principles study of molybdenum disulfide electronic structure *J. Phys.: Conf. Ser.* **877** 012026
[76] Zograf G, Polyakov A Y, Bancerek M, Antosiewicz T J, Küçüköz B and Shegai T O 2024 *Nat. Photon.* **18** 751–7
[77] Popkova A A *et al* 2022 *Laser Photon. Rev.* **16** 2100604
[78] Feng J, Wu Y K, Duan R, Wang J, Chen W, Qin J, Liu Z, Guo G C, Ren X F and Qiu C W 2024 *eLight* **4** 16
[79] Zhou X, Cheng J, Zhou Y, Cao T, Hong H, Liao Z, Wu S, Peng H, Liu K and Yu D 2015 *J. Am. Chem. Soc.* **137** 7994–7
[80] Schinke C *et al* 2015 *AIP Adv.* **5** 067168
[81] Garcia-Barrientos A, Bernal-Ponce J L, Plaza-Castillo J, Cuevas-Salgado A, Medina-Flores A, Garcia-Monterrosas M S and Torres-Jacome A 2021 *Materials* **14** 6349
[82] Narayanan K and Preble S F 2010 *Opt. Express* **18** 8998–9005
[83] Grinblat G 2021 *ACS Photon.* **8** 3406–32
[84] Hon N K, Soref R and Jalali B 2011 *J. Appl. Phys.* **110** 011301
[85] Xiong Y *et al* 2022 *Sci. Adv.* **8** eabo0375
[86] Connell G, Temkin R and Paul W 1973 *Adv. Phys.* **22** 643–65
[87] Yang T, Abdelwahab I, Lin H, Bao Y, Rong Tan S J, Fraser S, Loh K P and Jia B 2018 *ACS Photon.* **5** 4969–77
[88] Grinblat G, Li Y, Nielsen M P, Oulton R F and Maier S A 2016 *Nano Lett.* **16** 4635–40
[89] Youngblood N, Peng R, Nemilentsau A, Low T and Li M 2017 *ACS Photon.* **4** 8–14
[90] Wang T, Gai X, Wei W, Wang R, Yang Z, Shen X, Madden S and Luther-Davies B 2014 *Opt. Mater. Express* **4** 1011–22
[91] Jiang X *et al* 2018 *Laser Photon. Rev.* **12** 1700229
[92] Siefke T, Kroker S, Pfeiffer K, Puffky O, Dietrich K, Franta D, Ohlídal I, Szeghalmi A, Kley E B and Tünnermann A 2016 *Adv. Opt. Mater.* **4** 1780–6
[93] Guan X, Hu H, Oxenløwe L K and Frandsen L H 2018 *Opt. Express* **26** 1055–63
[94] Fu B, Sun J, Wang C, Shang C, Xu L, Li J and Zhang H 2021 *Small* **17** 2006054
[95] Castellanos-Gomez A *et al* 2014 *2D Mater.* **1** 025001
[96] Autere A, Jussila H, Dai Y, Wang Y, Lipsanen H and Sun Z 2018 *Adv. Mater.* **30** 1705963
[97] Lanzara A 2015 *Physics* **8** 91
[98] Kaelberer T, Fedotov V, Papasimakis N, Tsai D and Zheludev N 2010 *Science* **330** 1510–2
[99] Feng T, Xu Y, Zhang W and Miroshnichenko A E 2017 *Phys. Rev. Lett.* **118** 173901
[100] Wang Z, Lin R, Yao J and Tsai D P 2025 *npj Nanophoton.* **2** 4
[101] Radescu E and Vaman G 2002 *Phys. Rev. E* **65** 046609
[102] Miroshnichenko A E, Evlyukhin A B, Yu Y F, Bakker R M, Chipouline A, Kuznetsov A I, Luk'yanchuk B, Chichkov B N and Kivshar Y S 2015 *Nat. Commun.* **6** 8069
[103] Baryshnikova K V, Smirnova D A, Luk'yanchuk B S and Kivshar Y S 2019 *Adv. Opt. Mater.* **7** 1801350
[104] Zanganeh E, Evlyukhin A, Miroshnichenko A, Song M, Nenasheva E and Kapitanova P 2021 *Phys. Rev. Lett.* **127** 096804
[105] Babicheva V E and Evlyukhin A B 2017 *Laser Photon. Rev.* **11** 1700132
[106] Shamkhi H K, Baryshnikova K V, Sayanskiy A, Kapitanova P, Terekhov P D, Belov P, Karabchevsky A, Evlyukhin A B, Kivshar Y and Shalin A S 2019 *Phys. Rev. Lett.* **122** 193905
[107] Qin F, Zhang Z, Zheng K, Xu Y, Fu S, Wang Y and Qin Y 2022 *Phys. Rev. Lett.* **128** 193901
[108] Yang Y, Kravchenko I I, Briggs D P and Valentine J 2014 *Nat. Commun.* **5** 5753
[109] Sadrieva Z, Frizyuk K, Petrov M, Kivshar Y and Bogdanov A 2019 *Phys. Rev. B* **100** 115303
[110] Gladyshev S, Shalev A, Frizyuk K, Ladutenko K and Bogdanov A 2022 *Phys. Rev. B* **105** L241301
[111] Tan Z Q, Lin Q, Du W J, Wang L L and Liu G D 2025 *J. Appl. Phys.* **137** 033103
[112] Hsu C W, Zhen B, Lee J, Chua S L, Johnson S G, Joannopoulos J D and Soljačić M 2013 *Nature* **499** 188–91
[113] Monticone F and Alu A 2014 *Phys. Rev. Lett.* **112** 213903
[114] Sun G, Wang Y, Li Y, Cui Z, Chen W and Zhang K 2024 *Phys. Rev. B* **109** 035406
[115] Zhen B, Hsu C W, Lu L, Stone A D and Soljačić M 2014 *Phys. Rev. Lett.* **113** 257401
[116] Koshelev K, Tang Y, Li K, Choi D Y, Li G and Kivshar Y 2019 *ACS Photon.* **6** 1639–44
[117] Bernhardt N, Koshelev K, White S J, Meng K W C, Froch J E, Kim S, Tran T T, Choi D Y, Kivshar Y and Solntsev A S 2020 *Nano Lett.* **20** 5309–14
[118] Zograf G *et al* 2022 *ACS Photon.* **9** 567–74
[119] Koshelev K, Tang Y, Hu Z, Kravchenko I I, Li G and Kivshar Y 2023 *ACS Photon.* **10** 298–306
[120] Koshelev K, Lepeshov S, Liu M, Bogdanov A and Kivshar Y 2018 *Phys. Rev. Lett.* **121** 193903
[121] Tittl A, Leitis A, Liu M, Yesilkoy F, Choi D Y, Neshev D N, Kivshar Y S and Altug H 2018 *Science* **360** 1105–9
[122] Liu M, Powell D A, Guo R, Shadrivov I V and Kivshar Y S 2017 *Adv. Opt. Mater.* **5** 1600760
[123] Khardikov V V, Iarko E O and Prosvirnin S L 2010 *J. Opt.* **12** 045102
[124] Singh R, Al-Naib I A, Yang Y, Roy Chowdhury D, Cao W, Rockstuhl C, Ozaki T, Morandotti R and Zhang W 2011 *Appl. Phys. Lett.* **99** 201107
[125] Campione S *et al* 2016 *ACS Photon.* **3** 2362–7
[126] Vabishchevich P P, Liu S, Sinclair M B, Keeler G A, Peake G M and Brener I 2018 *ACS Photon.* **5** 1685–90
[127] Kühner L, Wendisch F J, Antonov A A, Bürger J, Hüttenhofer L, de S Menezes L, Maier S A, Gorkunov M V, Kivshar Y and Tittl A 2023 *Light Sci. Appl.* **12** 250
[128] Liu T, Qin M, Qiu J, Tu X, Qiu H, Wu F, Yu T, Liu Q and Xiao S 2025 *Nano Lett.* **25** 3646–52
[129] Luo X, Han Y, Du X, Chen S and Li G 2023 *Adv. Opt. Mater.* **11** 2301130
[130] Berté R, Weber T, de Souza Menezes L, Kühner L, Aigner A, Barkey M, Wendisch F J, Kivshar Y, Tittl A and Maier S A 2023 *Nano Lett.* **23** 2651–8
[131] Yesilkoy F, Arvelo E R, Jahani Y, Liu M, Tittl A, Cevher V, Kivshar Y and Altug H 2019 *Nat. Photon.* **13** 390–6
[132] Santiago-Cruz T, Gennaro S D, Mitrofanov O, Addamane S, Reno J, Brener I and Chekhova M V 2022 *Science* **377** 991–5
[133] You S *et al* 2023 *Nanophotonics* **12** 2051–60

[134] Fang C, Yang Q, Yuan Q, Gan X, Zhao J, Shao Y, Liu Y, Han G and Hao Y 2021 *Opto-Electron. Adv.* **4** 200030–1
[135] Zhou C, Huang L, Jin R, Xu L, Li G, Rahmani M, Chen X, Lu W and Miroshnichenko A E 2023 *Laser Photon. Rev.* **17** 2200564
[136] Liu Z, Xu Y, Lin Y, Xiang J, Feng T, Cao Q, Li J, Lan S and Liu J 2019 *Phys. Rev. Lett.* **123** 253901
[137] Huang L, Li S, Zhou C, Zhong H, You S, Li L, Cheng Y and Miroshnichenko A E 2024 *Adv. Funct. Mater.* **34** 2309982
[138] Zhou C, Zhou M, Fu Z, He H, Deng Z L, Xiang H, Chen X, Lu W, Li G and Han D 2025 *Nano Lett.* **25** 5916–24
[139] Watanabe K, Nagao T and Iwanaga M 2025 *Nano Lett.* **25** 2777–84
[140] Zhang X, Liu Y, Han J, Kivshar Y and Song Q 2022 *Science* **377** 1215–8
[141] Chen Y *et al* 2023 *Nature* **613** 474–8
[142] Anthur A P, Zhang H, Paniagua-Dominguez R, Kalashnikov D A, Ha S T, Maß T W, Kuznetsov A I and Krivitsky L 2020 *Nano Lett.* **20** 8745–51
[143] Liu Z, Wang J, Chen B, Wei Y, Liu W and Liu J 2021 *Nano Lett.* **21** 7405–10
[144] Wang Y, Pan Z, Yan Y, Yang Y, Zhao W, Ding N, Tang X, Wu P, Zhao Q and Li Y 2024 *Nanophotonics* **13** 3207–52
[145] Yang M, Weissflog M A, Fedorova Z, Barreda A I, Börner S, Eilenberger F, Pertsch T and Staude I 2024 *Nanophotonics* **13** 3311–9
[146] Fedotova A, Younesi M, Sautter J, Vaskin A, Löchner F J, Steinert M, Geiss R, Pertsch T, Staude I and Setzpfandt F 2020 *Nano Lett.* **20** 8608–14
[147] Carletti L, Zilli A, Moia F, Toma A, Finazzi M, De Angelis C, Neshev D N and Celebrano M 2021 *ACS Photon.* **8** 731–7
[148] Semmlinger M, Tseng M L, Yang J, Zhang M, Zhang C, Tsai W Y, Tsai D P, Nordlander P and Halas N J 2018 *Nano Lett.* **18** 5738–43
[149] Das Gupta T, Martin-Monier L, Butet J, Yang K Y, Leber A, Dong C, Nguyen-Dang T, Yan W, Martin O J and Sorin F 2021 *Nanophotonics* **10** 3465–75
[150] Abdelraouf O A, Anthur A P, Wang X R, Wang Q J and Liu H 2024 *ACS Nano* **18** 4388–97
[151] Xu L *et al* 2019 *Adv. Sci.* **6** 1802119
[152] Gao J, Vincenti M A, Frantz J, Clabeau A, Qiao X, Feng L, Scalora M and Litchinitser N M 2021 *Nat. Commun.* **12** 5833
[153] Gandolfi M, Tognazzi A, Rocco D, De Angelis C and Carletti L 2021 *Phys. Rev. A* **104** 023524
[154] Shi T *et al* 2022 *Nat. Commun.* **13** 4111
[155] Tonkaev P, Toftul I, Lu Z, Qin H, Qiu S, Yang W, Koshelev K, Lu Y and Kivshar Y 2024 *Nano Lett.* **24** 10577–82
[156] Xiao S, Qin M, Duan J and Liu T 2022 *Opt. Express* **30** 32590–9
[157] Lu Y W, Li W and Wang X H 2025 *ACS Nano* **19** 17953–78
[158] Lu Y W 2024 *Phys. Rev. A* **110** 033720
[159] Lu Y W, Zhou W J, Li Y, Li R, Liu J F, Wu L and Tan H 2022 *Nanophotonics* **11** 3307–17
[160] Liu H, Guo C, Vampa G, Zhang J L, Sarmiento T, Xiao M, Bucksbaum P H, Vučković J, Fan S and Reis D A 2018 *Nat. Phys.* **14** 1006–10
[161] Jangid P, Richter F U, Tseng M L, Sinev I, Kruk S, Altug H and Kivshar Y 2024 *Adv. Mater.* **36** 2307494
[162] Shcherbakov M R *et al* 2021 *Nat. Commun.* **12** 4185
[163] Tonkaev P, Lai F, Kruk S, Song Q, Scalora M, Koshelev K and Kivshar Y 2024 *Phys. Rev. Res.* **6** 033073
[164] Zhao Y, Chen Z, Wang C, Yang Y and Sun H B 2023 *Nanoscale* **15** 12926–32
[165] Zhang J, Ma J, Parry M, Cai M, Camacho-Morales R, Xu L, Neshev D N and Sukhorukov A A 2022 *Sci. Adv.* **8** eabq4240
[166] Ma J, Zhang J, Jiang Y, Fan T, Parry M, Neshev D N and Sukhorukov A A 2023 *Nano Lett.* **23** 8091–8
[167] Zhang J, Ma J, Li N, Lung S and Sukhorukov A A 2024 *Optica* **11** 753–8
[168] Ma J, Ren J, Zhang J, Meng J, McManus-Barrett C, Crozier K B and Sukhorukov A A 2025 *eLight* **5** 2
[169] Ma J *et al* 2025 *Sci. Adv.* **11** eadu4133
[170] Wang K, Chekhova M and Kivshar Y 2022 *Phys. Today* **75** 38–44
[171] Mazzanti A, Parry M, Poddubny A N, Della Valle G, Neshev D N and Sukhorukov A A 2022 *New J. Phys.* **24** 035006
[172] Lyu X, Kallioniemi L, Hong H, Qu R, Zhang Y, Zúñiga-Perez J, Liu K and Gao W 2025 *Nat. Commun.* **16** 1899
[173] Liang H, Gu T, Lou Y, Yang C, Ma C, Qi J, Bettiol A A and Wang X 2025 *Sci. Adv.* **11** eadt3710
[174] Fan T *et al* 2025 *Nano Lett.* **25** 11844–51
[175] Sultanov V, Santiago-Cruz T and Chekhova M V 2022 *Opt. Lett.* **47** 3872–5
[176] Camacho-Morales R, Xu L, Zhang H, Ha S T, Krivitsky L, Kuznetsov A I, Rahmani M and Neshev D 2022 *Nano Lett.* **22** 6141–8
[177] Moretti G Q, Weber T, Possmayer T, Cortés E, Menezes L d S, Bragas A V, Maier S A, Tittl A and Grinblat G 2024 *Nanophotonics* **13** 3421–8
[178] Khurgin J B 2022 *ACS Photon.* **9** 743–51
[179] Tonkaev P, Sinev I S, Rybin M V, Makarov S V and Kivshar Y 2022 *Chem. Rev.* **122** 15414–49
[180] Chen M K, Liu X, Sun Y and Tsai D P 2022 *Chem. Rev.* **122** 15356–413
[181] Fan Y *et al* 2022 *Laser Photon. Rev.* **16** 2100425
[182] Hentschel M, Koshelev K, Sterl F, Both S, Karst J, Shamsafar L, Weiss T, Kivshar Y and Giessen H 2023 *Light Sci. Appl.* **12** 3
[183] Huang S H, Su H P, Chen C Y, Lin Y C, Yang Z, Shi Y, Song Q and Wu P C 2024 *Nat. Commun.* **15** 9658